2020

Generalized Optimal Control for Autonomous Mine Countermeasures Missions

Kragelund, Sean; Walton, Claire; Kaminer, Isaac; Dobrokhodov, Vladimir

IEEE

Peer-Reviewed Technical Communication

Generalized Optimal Control for Autonomous Mine Countermeasures Missions

Sean Kragelund, Claire Walton, Isaac Kaminer, and Vladimir Dobrokhodov

***Abstract*—This article presents a computational framework for planning mine countermeasures (MCM) search missions by autonomous vehicles. It employs generalized optimal control (GenOC), a model-based trajectory optimization approach, to maximize the expected search performance of vehicle–sensor pairs in different minehunting scenarios. We describe each element of the proposed framework and adapt it to solve real-world MCM motion planning problems. A key contribution of this article develops sensor models that are more tunable than conventional ones based on lateral range curves. The proposed models incorporate engineering parameters and 3-D geometry to compute mine detection probability as a function of sonar design and search vehicle trajectories. Specific examples for various forward-looking and sidescan sonar systems deployed by unmanned vehicles are included. Objective computations utilize these sonar detection models during optimization to minimize the risk that candidate search trajectories fail to detect mines in an area of interest. Simulation results highlight the flexibility of our proposed GenOC framework and confirm that optimal trajectories outperform conventional search patterns under time or resource constraints. We conclude by identifying some of the practical considerations of this approach, and suggest ways that numerical analysis of GenOC solutions can be used for MCM mission planning and decision aid development.**

***Index Terms*—Autonomous underwater vehicle (AUV), autonomous vehicles, mine countermeasures (MCM), motion planning, optimal control, unmanned surface vessel (USV), unmanned vehicles.**

I. Introduction

OVER the last two decades, unmanned vehicle systems have grown steadily more capable, reliable, and ubiquitous. As system designers increasingly turn to commercial technologies and open architectures, it is easier than ever for robotic systems to interoperate. As a result, multiple dissimilar vehicles can be combined into a collaborative team to overcome individual vehicle limitations and deliver advanced capabilities—even across operating domains. Autonomous vehicle teams have great potential in a wide range of scientific, commercial, and defense applications, and they are especially well suited for remote sensing in maritime domains.

To maximize the utility of a heterogeneous vehicle team for a given sensing mission, motion planning algorithms must consider the capabilities and limitations of each team member. At a minimum, they should incorporate dynamic and operational constraints to produce feasible trajectories. Optimization techniques can be used to allocate effort according to individual vehicles' sensor performance. Such techniques can produce motion plans that are superior to conventional "lawnmower" survey patterns, which may be suboptimal for certain sensors and infeasible for underactuated vehicles to follow precisely.

Autonomous systems must also operate with imperfect information about their environment. This is particularly true in the maritime domain, where sensor accuracy usually depends on acoustical conditions and vehicle motion may be subject to unknown disturbances at the water surface. In underwater search applications, the ability to detect and localize a target with sonar is impacted by several factors including acoustical noise, ambiguous geometry, and aspect dependence. Consequently, the performance of an autonomous system may depend greatly on its ability to cope with uncertainty. Motion planning algorithms that consider uncertainty, therefore, can increase a system's overall robustness. Generalized optimal control (GenOC) is a model-based computational framework for optimizing vehicle trajectories in the face of uncertainty. This article describes the GenOC approach to motion planning in detail, greatly elaborating on initial results first reported in [1], using a practical example: planning optimal minehunting missions for autonomous vehicle teams.

A. Mine Countermeasures (MCM)

There are a number of complex sensing missions that could utilize autonomous vehicle teams to deliver a mix of different capabilities, particularly in environments that pose a risk to humans. The U.S. Navy has embraced this vision, and invested heavily in vehicle and sensor technologies for MCM. These operations traditionally comprise both minesweeping and minehunting tasks. The goal of minesweeping is "to cause the mine's sensors to detonate the mine in circumstances where the detonation is harmless" [2, p. 169]. Minehunting, however, attempts to locate, then avoid or destroy the mine through other means. Nevertheless, "sweeping and hunting are both essentially search problems" [2, p. 169].

Minehunting operations are conducted in a sequence of phases [3], each performed by various types of vehicles and sensors [4]. Presently, these assets require dedicated support from manned platforms, but a current thrust of naval research is aimed at enabling autonomous systems to support other unmanned vehicles during MCM operations [5], [6]. Fig. 1 shows a *SeaFox* unmanned surface vessel (USV) and a remote environmental monitoring units (REMUS) 100 autonomous underwater vehicle (AUV), two of the fleet-representative vehicles used at the Naval Postgraduate School (NPS) Center for Autonomous Vehicle Research (CAVR), Monterey, CA, USA. In this article, we consider sensor-based motion planning strategies for a heterogeneous team comprised of these types of vehicles conducting autonomous minehunting missions.

Minehunting missions are often conducted in the following three distinct phases:

Manuscript received October 19, 2018; revised September 27, 2019 and March 6, 2020; accepted May 25, 2020. This work was supported in part by the Naval Research Program and the Consortium for Robotics and Unmanned Systems Education and Research at the Naval Postgraduate School, and in part by the Office of Naval Research Science of Autonomy program. This article was presented in part at the MTS/IEEE OCEANS Conference, Monterey, CA, USA, September 19–23, 2016. *(Corresponding author: Sean Kragelund.)*

Associate Editor: F. Zhang.

The authors are with the Department of Mechanical and Aerospace Engineering, Naval Postgraduate School, Monterey, CA 93943 USA (e-mail: spkragel@nps.edu; clwalton1@nps.edu; kaminer@nps.edu; vndobrok@nps.edu).

Digital Object Identifier 10.1109/JOE.2020.2998930

Fig. 1. NPS *SeaFox* USV and REMUS 100 AUV.

1) wide area detection, classification, and localization (DCL) of minelike objects (MLOs) with long-range low-resolution sensors;
2) reacquisition and identification (RID) with short-range high-resolution sensors;
3) neutralization of identified mines [7].

Phases one and two increasingly utilize autonomous vehicles, whereas phase three typically requires EOD divers and/or remotely operated vehicles. Therefore, this article will focus on the first two phases. Furthermore, the literature describes several different approaches for planning MCM missions with autonomous vehicles, including automated scheduling methods that optimize over vehicle resources to complete a sequence of MCM tasks (e.g., [6]). In this article, however, we concentrate on sensor-based motion planning algorithms, which compute trajectories for individual vehicles to follow.

B. Motion Planning for Autonomous Minehunting Missions

Phase one is typically treated as a coverage problem [7]–[9], especially when there is no prior information about mine locations. Large search areas are usually subdivided into smaller regions, which can be covered by a typical AUV mission duration [8], or subdivided by bottom type [10], so that different sensors, track spacing, etc., can be tailored to the local environment. Several coverage path planning methods may be used, but vehicle plans for this phase are usually based on deterministic and exhaustive coverage exemplified by the popular lawnmower pattern.

Phase two can be thought of as a targeted coverage problem, guided by prior information about the expected target locations. When a vehicle must visit multiple MLOs during an RID mission, this is akin to solving a traveling salesman problem [9] to visit each target location. Typically, a "standard" multiple aspect coverage pattern comprising parallel tracks at different headings is then executed above each target. This method ensures that high-resolution imagery is collected from several different aspect angles to aid the identification effort. Often, the choice of sensor dictates the type of vehicle paths considered for RID missions. Sidescan sonar (SSS), for example, does not produce good imagery when the search platform does not follow level, straight line paths. Therefore, these planning methods do not consider vehicle dynamics beyond speed, minimum turning radius, and/or the time required to make a turn. Some methods account for the distance required to stabilize on the next track line after making a U-turn [11]. When planning lawnmower coverage patterns for SSS, still other algorithms optimize over the space of track line headings [12], [13].

Optimal control is an alternative motion planning technique, which provides a mathematical framework for solving problems with dynamic constraints and different performance criteria. Recent developments in numerical methods have made it possible to explicitly incorporate parameter uncertainty into the objective function of an optimal control problem [14]–[17]. This situation arises when conducting an optimal search for stationary targets at unknown locations, or when searching for mobile targets whose motion can be conditionally determined by an uncertain parameter. These so-called GenOC problems can incorporate sensor performance models to produce optimal vehicle trajectories for a given sensor configuration. Researchers have successfully applied these methods to solve motion planning problems in continuous time and space with complex and multiagent interactions in a variety of scenarios including optimal search, path coverage, and force protection [18]. This motion planning method will be employed for the rest of this article.

C. Sensor Performance

To address vehicle- and sensor-specific motion planning problems considered in this article, we must first develop probabilistic models for two classes of sensors routinely deployed during MCM operations: forward-looking sonar (FLS) and SSS. While these sonar systems can differ widely according to their intended application, they share several common characteristics. First, both forward-looking sonar (FLS) and SSS are examples of active sonar. That is, they transmit acoustical signals into the water and process the echoes reflected from objects in the environment to detect their presence. For a given sonar, this process occurs at an average rate, so detection performance depends on time. Second, active sonar systems employ transmit/receive arrays of transducers to improve detection performance in a desired direction and often add acoustical baffling to reject echoes from unwanted directions. A sonar design's array geometry therefore produces an effective field of view (FOV) within which targets can be reliably detected, so detection performance also depends on a sonar's orientation relative to targets in the environment. Last, since these sonar systems are rigidly mounted onto a vehicle platform, the sonar's orientation ultimately depends on that vehicle's trajectory through the search area. This trajectory defines the position, orientation, and velocity of the vehicle as a function of time. Since these quantities are constrained by the vehicle's equations of motion (EOM), we note that a sonar's overall detection performance is a function not only of its design parameters but also its vehicle platform dynamics.

Assuming that detection performance defines sonar's effectiveness for a given mission, this metric can be generalized to any sonar. That is, a mission to detect and localize mines with a long-range low-resolution sonar has the same objective as a mission to reacquire and identify these mines with a high-resolution sonar. We assume that detection with such a sonar is sufficient for successful identification to occur. Under these assumptions, sensor-based motion planning algorithms for MCM should employ sonar detection models with the following characteristics.

1) Detection probability reflects an actual sonar's dependence on array design, vehicle dynamics, and 3-D search geometry. In this way, simulation can serve as a powerful tool to evaluate the effectiveness of different sonar designs deployed from various vehicle platforms.
2) Simulated detection performance agrees with the expected/observed performance of actual sonar. This can be assessed by model verification and validation.
3) Detection functions permit rapid calculations within numeric optimization routines. This requires tradeoffs between accuracy and execution speed. Smooth and differentiable functions with analytic gradients, for example, significantly reduce solution times when using gradient-based optimization.

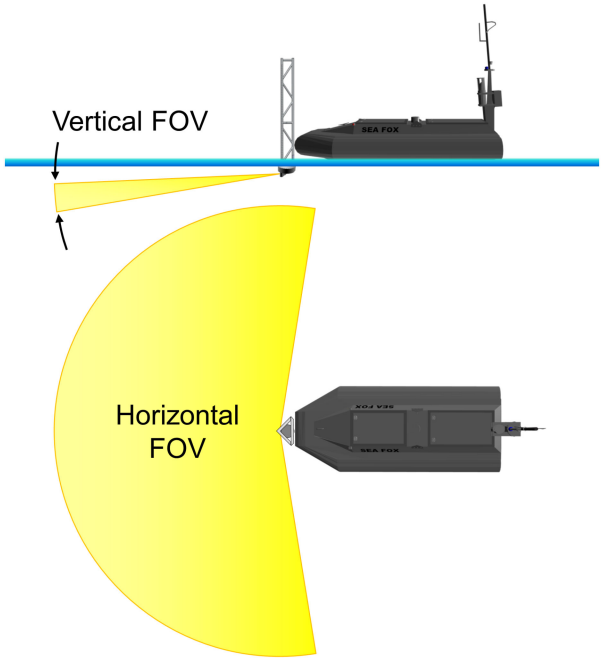

Fig. 2. FOVs for a USV bow-mounted FLS.

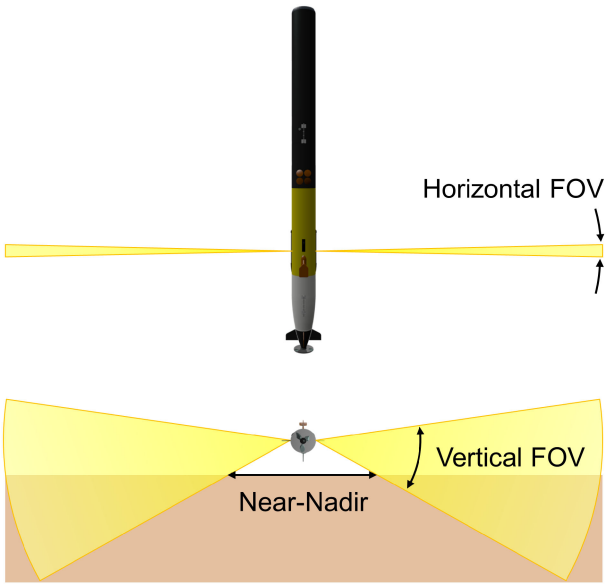

Fig. 3. FOVs and near-nadir region for an AUV SSS.

Many sensor models commonly used in search theory are chosen for their computational simplicity and do not satisfy all of these desired characteristics. Most ignore 3-D geometry, for example, but this can greatly impact detection performance when searching for mines on the seafloor with a surface craft's FLS (see Fig. 2) or an underwater vehicle's SSS. It is also well known that SSS cannot detect targets located directly beneath a vehicle's path of travel, in the so-called near-nadir region (see Fig. 3). For this reason, overlapping sensor swaths is required to obtain complete coverage with this sensor [19].

Definite range models, or "cookie cutter" sensors, simply assume that detection is certain within a fixed range of the sensor and impossible outside it. Washburn and Kress note the appeal of such a model for

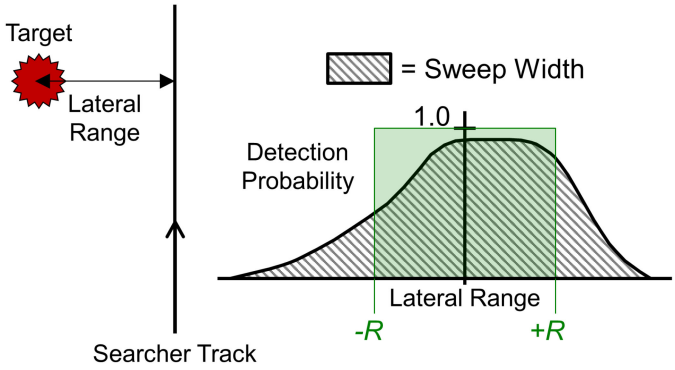

Fig. 4. Lateral range curves and sweep widths for a typical sensor (black) and a definite range sensor (green). Adapted from [2].

analysis, but acknowledge that "attempts to forecast fixed ranges in the real world are often disappointing," remarking that "forecast detection ranges for sonars are notoriously subject to error—it is not uncommon to be off by a factor of two or more" [2, p. 135].

One alternative to definite range models are so-called lateral range curves. This approach graphs a sensor's detection probability as a function of lateral range, defined as the distance from a searcher's straight line track at its point of closest approach to a target. The area under a sensor's lateral range curve defines its sweep width, a measure of sensor effectiveness used when planning to search an area with evenly spaced track lines, e.g., with a lawnmower coverage pattern [20]. Lateral range curves can be derived analytically, assuming detection rate is proportional to range via an inverse cube law, or derived empirically via repeated experiments [21], [22].

Fig. 4 depicts the lateral range curve and corresponding sweep width for a typical sensor and for the special case of a definite range sensor with radius R overlaid in green. We note that, in general, both sensor models produce maximum detection probabilities at target ranges approaching zero. While appropriate for optical sensors (one of the original motivations for deriving the inverse cube law in World War II), these models usually require modifications to accurately simulate sensors such as SSS.

One example of a sensor profile used to approximate the expected gap in SSS coverage (see Fig. 5) is presented in [11]. This model modifies a "cookie cutter" sensor by adding a "blind zone" of zero detection probability in the near-nadir region below the vehicle. The resulting sensor profile is shown in Fig. 6. This model is well suited for this specific application, namely finding an optimal track line location that maximizes the probability of detecting targets for a given heading, but it does not generalize well to other applications. Furthermore, this sensor model does not depend explicitly on vehicle dynamics; the knowledge that SSS performs better when its vehicle platform follows straight line tracks is implicit in the problem formulation, which considers only straight path segments.

An engineering-based approach to modeling sensors, such as radar and sonar, calculates "signal excess" (SE) from physical models of the sensor and its operating environment to determine when detection is possible [21], [22]. Moreover, the Poisson Scan model described in [21] and [24] can be used to derive a sensor's detection rate. Sensor models of this form are used to solve optimal search problems in [16], [18], and [25], although these models implement a much simpler approximation of an actual SE equation. Nevertheless, Walton *et al.* [26] described how models based on rate functions can be calibrated to "shape" their performance and solve a wide variety of problems, highlighting the flexibility of this modeling approach.

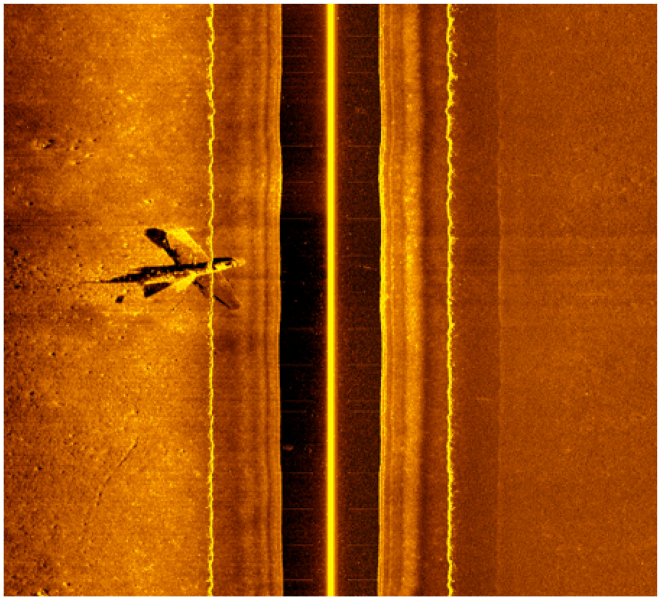

Fig. 5. SSS image showing near-nadir coverage gap. Source: [23].

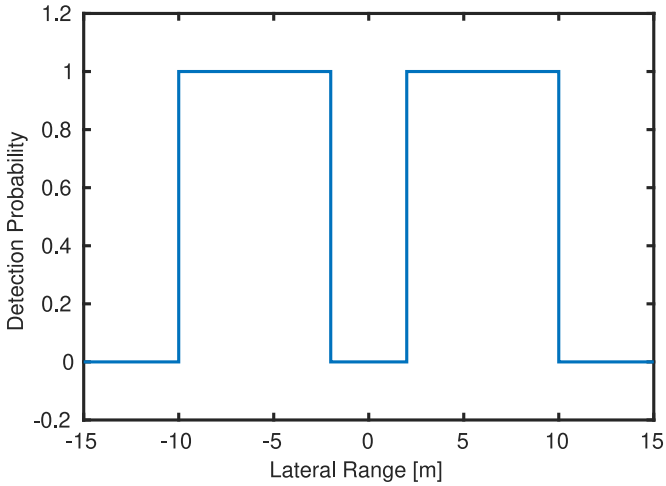

Fig. 6. Definite range sensor profile with near-nadir gap. Adapted from [11].

This article describes how to utilize a novel GenOC technique as a mission planning tool for a team of dissimilar vehicles conducting DCL and RID missions for MCM. Section II introduces the main components of this model-based computational framework. Section III presents a detailed derivation of the sonar models used to simulate the detection performance of various minehunting sonars deployed from USVs and AUVs. The main technical contribution is an SE model that incorporates sonar design parameters and 3-D geometery to compute detection probability as a function of a vehicle's trajectory. Results from computer simulations, which highlight the flexibility and utility of this solution framework for different minehunting missions under resource constraints, are presented in Section IV, with additional numerical analysis provided in Section V.

II. GenOC Problem Formulation

In this article, we cast different MCM operations as optimal search problems whose solutions yield motion plans for a team of autonomous vehicles. We specifically consider two MCM missions: first, an initial wide area survey with long-range low-resolution sonar to detect and locate MLOs; and second, a subsequent mission to revisit these locations with high-resolution sonar for positive target identification. An objective function is defined, which can incorporate different searcher, sensor, and target distribution models to solve different MCM search problems, demonstrating the flexibility of the GenOC framework.

A number of vehicles and sensors are capable of performing the search tasks described earlier, but mission planners must consider which combinations are most effective for a given MCM operation. Often, the available vehicle platform dictates which sensors can be utilized, whereas a sensor may dictate the type of trajectory a vehicle must follow. We assume in this work that each vehicle deploys only one type of sonar, but acknowledge that some developmental systems can carry multiple sophisticated sonars at once [4], [27]. Another characteristic of search operations is that prior information (or the lack thereof) about potential target locations influences how the search is planned and executed.

The GenOC framework includes all of these characteristics: multivehicle operations, sensor-based motion planning, and prior information. It can be customized to explore a wide variety of MCM scenarios simply by swapping different models of vehicle/sensor performance and initial target distribution. The benefits of this approach are twofold: solutions not only specify trajectories that each vehicle can execute to optimize performance of a given sensor payload, but they also establish performance benchmarks for a given problem, as discussed in Sections IV and V.

The remainder of this section describes the mathematical models and the objective function used to solve MCM search scenarios within the GenOC framework.

A. Searcher Models

The search vehicles selected for a given mission constrain the admissible solutions to an optimal control problem. Specifically, we define a mathematical model for a vehicle's dynamic EOM. This model relates a vector of n_x state variables $\vec{\mathbf{x}}(t) \in \mathbb{R}^{n_x}$ and a vector of n_u control inputs $\vec{\mathbf{u}}(t) \in \mathbb{R}^{n_u}$ through a set of ordinary differential equations (ODEs) in state-space form: $\dot{\vec{\mathbf{x}}}(t) = \vec{\mathbf{f}}(\vec{\mathbf{x}}(t), \vec{\mathbf{u}}(t))$. This model places dynamic constraints on how the states may evolve with time. Similarly, physical actuator limitations place algebraic constraints on the control inputs: $\vec{\mathbf{u}}_{\min} \leq \vec{\mathbf{u}}(t) \leq \vec{\mathbf{u}}_{\max}, \forall t \in [0, T_f]$. Operational constraints may further bound the region of state space explored during optimization: $\vec{\mathbf{x}}_{\min} \leq \vec{\mathbf{x}}(t) \leq \vec{\mathbf{x}}_{\max}, \forall t \in [0, T_f]$. We note that for multivehicle problems with n_v searchers, the state and control vectors are augmented to include the states and controls of all vehicles, $\vec{\mathbf{x}}(t) \in \mathbb{R}^{n_v \times n_x}$ and $\vec{\mathbf{u}}(t) \in \mathbb{R}^{n_v \times n_u}$, respectively. Sections II-A1 and II-A2 describe two vehicle models that are representative of autonomous platforms being used for MCM.

1) SeaFox USV: The Naval Postgraduate School (NPS) *SeaFox* USVs are small 5-m rigid hull inflatable boats originally designed for remote-controlled intelligence, surveillance, reconnaissance, force protection, and maritime interdiction operations (MIOs) conducted by the U.S. Navy and the U.S. Coast Guard [28], [29]. CAVR has converted these vessels into fully autonomous surface craft in support of various research programs, including sonar-based path planning for riverine navigation [30], [31] and precise speed control [32]. More recently, CAVR modified its *SeaFox* Mk II USV to deploy the autonomous topographic large area sonar (ATLAS) minehunting FLS for MCM research [33].

To develop a model for these vehicles, we assume that USVs conduct MCM search missions at constant velocity, without aggressive maneuvers, and therefore exhibit simple planar motion at the sea surface (i.e.,

TABLE I
DESIGN PARAMETERS FOR A USV MODEL

Design Parameter	SeaFox Value
Nomoto Gain Constant, K	0.5 1/s
Nomoto Time Constant, T	5.0 s
Velocity, V	2.5 m/s

TABLE II
DESIGN PARAMETERS FOR AN AUV MODEL

Design Parameter	REMUS 100 Value
Nomoto Gain Constant, K	2.0 1/s
Nomoto Time Constant, T	1.0 s
Velocity, V	1.5 m/s

pitch, roll, and heave motions are zero). If we further assume that sway motions are negligible (i.e., sideslip is zero), the EOM can be adequately modeled by kinematics. Let the state variable pair $[x(t), y(t)]$ be the vehicle's position in meters north and east from an inertial reference frame, $\psi(t)$ be its heading angle in radians measured clockwise from north, and $r(t)$ be its turn rate in radians per second. If the vehicle travels at constant forward velocity V meters per second, the state–space EOM for the state vector $\vec{\mathbf{x}}(t) \equiv [x(t), y(t), \psi(t), r(t)]^\top$ and control input $u(t)$ are

$$\begin{aligned} \dot{x}(t) &= V \cos\psi(t) \\ \dot{y}(t) &= V \sin\psi(t) \\ \dot{\psi}(t) &= r(t) \\ \dot{r}(t) &= \frac{1}{T}\left(K u(t) - r(t)\right). \end{aligned} \tag{1}$$

Equation (1) implements a first-order approximation to the well-known Nomoto model for ship-steering equations, a simple transfer function between rudder deflection angle $u(t) = \delta_r(t)$ and turn rate $r(t)$ that "is the most popular model used for ship autopilot design due to its simplicity and accuracy" [34, p. 309]. The Nomoto gain constant *K* (in s^{-1}) and time constant *T* (in s) can be identified from sea trial maneuvers as described in [35]–[38]. Table I lists the values of *V*, *K*, and *T* used in our *SeaFox* USV model.

2) REMUS 100 AUV: The REMUS 100 AUV is a small and rapidly deployable unmanned underwater vehicle for collecting environmental data in the ocean [39]. Its modular design accommodates a number of different sensors for hydrographic survey missions, and its SSS system can make detailed maps of the ocean floor. Being one of the first AUVs adopted for naval MCM operations [19], [40], REMUS vehicles were used during Operation Iraqi Freedom in 2003 [41]. The REMUS family of vehicles includes two MCM variants in use by the Navy today: the MK 18 Mod 1 Swordfish, based on the 7.5-in diameter REMUS 100, and the MK 18 Mod 2 Kingfish, based on the 12.75-in diameter REMUS 600 [42]. CAVR operates three REMUS 100 AUVs in support of its research programs, and has been developing sensor-based navigation algorithms that utilize blazed array FLS since 2004 [43]–[45].

AUVs can move in all three dimensions, and six degrees of freedom (DOF) are required to describe this motion completely. An example of a full six-DOF model for simulating the nonlinear dynamics of a REMUS 100 is presented in [46]. In practice, however, these EOM are usually decoupled into separate and linearized equations in the horizontal and vertical planes so that designers can develop controllers for steering and diving, respectively. For our search problem, since AUVs typically conduct constant-velocity SSS surveys at a fixed altitude above the bottom, we consider only 2-D planar motion. Finally, as a matter of convenience when implementing multivehicle problems in software, we prefer a motion model with the same form as the *SeaFox* USV model in Section II-A1. This provides easier state vector indexing when AUVs and USVs operate together in a heterogeneous vehicle team.

Under the same assumptions of zero pitch, roll, and heave motion, we derive a Nomoto steering model for the REMUS 100 AUV from the linearized, decoupled, and lateral steering equations in [46, eq. (118)], as shown in Appendix A. Using the *SeaFox* sign convention, we calculate the parameters for our REMUS 100 model listed in Table II.

Since our MCM scenario concerns the search for bottom mines, a vehicle's altitude h above the seafloor must also be specified for a given mission. For surface craft, altitude h equals the water depth itself, due to our flat bottom constant depth assumptions.

B. Sensor Models

Engineering-based sensor models for different types of active sonar used in MCM are developed in Section III. These models calculate the instantaneous probability p that a given sonar can detect an echo from a specific target against the expected ambient noise level. This quantity is a function of the sonar design, parameterized by its figure of merit (FOM), and the two-way propagation losses (PLs) between the sonar and target when a scan occurs. For a given sonar, this process occurs at an average rate λ, producing the instantaneous detection rate γ. At these scan times, instantaneous detection probability also depends on whether the target lies within the sonar's FOV, which depends on 3-D geometry relative to the search vehicle trajectory $\vec{\mathbf{x}}(t)$. Scalar shaping functions F_α and F_ε are designed to characterize geometric relationships based on azimuth and elevation angle, respectively, to a target location $\vec{\boldsymbol{\omega}}$. Likewise, shaping function F_r is designed to reflect the influence of vehicle turn rate. Table III lists all the expressions used to compute these terms and yield the instantaneous detection rate

$$\gamma(\vec{\mathbf{x}}(t), \vec{\boldsymbol{\omega}}) = \lambda\, p(\vec{\mathbf{x}}(t), \vec{\boldsymbol{\omega}})\, F_\alpha(\vec{\mathbf{x}}(t), \vec{\boldsymbol{\omega}})\, F_\varepsilon(\vec{\mathbf{x}}(t), \vec{\boldsymbol{\omega}})\, F_r(\vec{\mathbf{x}}(t)). \tag{2}$$

C. Target Models

The GenOC framework was developed to address optimal control problems with parameter uncertainty [14], [17], [18]. For the MCM search problems considered in this article, the uncertain parameter is the location of a mine target on the seafloor. We assume, therefore, that target location is a stochastic parameter $\vec{\boldsymbol{\omega}}$ distributed over a search area $\boldsymbol{\Omega}$ according to a known continuous probability density function (pdf): $\phi(\vec{\boldsymbol{\omega}}) : \boldsymbol{\Omega} \mapsto \mathbb{R}$. That is, $\vec{\boldsymbol{\omega}} \in \boldsymbol{\Omega} \subset \mathbb{R}^{n_\omega}$ [14], and $n_\omega = 2$. Different pdfs allow a number of possible target distributions that produce different solutions to the optimal search problem.

Two specific target distribution models are used to simulate two MCM missions. During the initial phase of an MCM operation, for example, wide area surveys are conducted to detect and localize MLOs in a given search area. We formulate this task as an optimal search problem where no prior target data are available. We therefore model this target distribution with a joint uniform pdf, bounded by the search area coordinates. This pdf contains no exploitable information, i.e.,

TABLE III
TERMS USED TO COMPUTE INSTANTANEOUS DETECTION RATE

Symbol	Definition	Cross Reference
SE	Signal Excess	(14)
FOM	Figure of Merit	(15)
PL	Propagation Loss	(17)
p	Probability of Detection	(19)
λ	Poisson Scan Rate	Section III-C
F_α	Azimuth Shaping Function	
	Forward-looking Sonar	(23)
	Sidescan Sonar	(26)
F_ε	Elevation Shaping Function	(24)
F_r	Turn Rate Shaping Function	(27)

there is an equal probability of finding a target anywhere within the search area. This noninformative target model, representing only a single mine which must be located, nevertheless combines with the objective function defined in Section II-D to generate trajectories that maximize sensor coverage in the time available, effectively solving a coverage problem. A search vehicle that follows these trajectories would be expected to detect all MLOs present in the covered area, and their locations would be used to plan contact investigation missions.

In subsequent phases of an MCM operation, follow-on sorties are conducted to reacquire previously detected MLOs and identify mines from nonmine/mine-like bottom objects using high-resolution sonar. We therefore formulate each RID task as another single-target optimal search problem, each with potentially different vehicle and sensor models. These missions utilize MLO location data gathered during a previous survey, but the accuracy of prior information is commensurate with the survey vehicle's navigation performance. This variation can be modeled with any continuous pdf. Walton, however, suggested the use of joint normalized beta distributions for this task. These distributions allow simple manipulation and customization via their α, β shape parameters, and benefit from a finite radius of effectiveness [26]. The pdf for the beta distribution, defined for $x \in [0, 1]$, $\alpha > 0$, and $\beta > 0$ [47], is

$$\phi(x; \alpha, \beta) = \frac{1}{B(\alpha, \beta)} x^{\alpha-1} (1-x)^{\beta} - 1 \tag{3}$$

where

$$B(\alpha, \beta) = \frac{(\alpha-1)!\,(\beta-1)!}{(\alpha+\beta-1)!}.$$

Section IV illustrates how the probabilistic target models described earlier produce search vehicle trajectories for both wide area DCL surveys (see Section IV-A) and RID missions (see Section IV-B). Our approach, however, does not currently address one classical objective of MCM: estimating the number of mines remaining in an area after clearance operations. A number of methods for quantifying this risk are described in the literature, e.g., [48]–[50]. These methods combine probabilistic assumptions about the number of mines initially present, their distribution within the search area, and how to update these quantities based on search results. Our future work will address ways to incorporate probabilistic updates into the GenOC framework for continuous replanning based on target detection and identification events.

D. Objective Function

In this section, we present the exponential detection model, first described in [51], which is commonly used to quantify search performance in continuous time. Based on a sensor's instantaneous detection rate (see Section III-C), this model provides a convenient objective function for optimal search problems, with recent examples provided in [14], [15], and [18]. For our problem, we define *residual MCM risk* as the probability that a team of autonomous vehicles fails to detect the mines in a search area by the end of an MCM operation. This scalar quantity can be readily calculated for a given set of vehicle and sonar capabilities, and also reflects the time available for search. Therefore, we utilize MCM risk as the objective function for our optimal search problems; minimizing this quantity maximizes the mission's probability of success.

Given an instantaneous detection rate $\gamma(t)$, derivation of the exponential detection model proceeds from the following two assumptions [51]:

1) the probability of detection in the short time interval $[t, t + \Delta t]$ is $\gamma(t)\,\Delta t$;
2) detection events in all such nonoverlapping time intervals are independent.

Washburn cautions that the independence assumption may not hold in all situations. For example, consecutive detection failures due to low SE could be caused by low target strength (TS) or poor acoustical conditions. Empirically, however, these assumptions "provide good approximations in a wide variety of circumstances" [21, Ch. 2, p. 3]. Koopman acknowledges the importance of recognizing when this assumption is legitimate, and justifies its use beyond cases of random search.

> The assumption is in fact legitimate—and important—when applied to *conditional probabilities* of detection: probabilities calculated on the basis of *postulated* positions and motions of the target. [52]

This is precisely the case described by our objective function for MCM risk in (8), which we now derive using Koopman's "assumption of independence."

Let $p(t)$ be the probability of detection at time t. Then, by the complement, the probability of a detection *failure* is $q(t) = 1 - p(t)$. Under our stated assumptions, this probability becomes $q(t + \Delta t) = q(t)\,(1 - \gamma(t)\,\Delta t)$ at the end of the next scan interval, which can be rearranged as the difference equation

$$\frac{q(t+\Delta t) - q(t)}{\Delta t} = -q(t)\,\gamma(t). \tag{4}$$

In the limit as $\Delta t \to 0$, we obtain the differential equation

$$\dot{q}(t) = -q(t)\,\gamma(t) \tag{5}$$

which has the closed-form solution

$$q(t) = e^{-\int_0^t \gamma(\tau)\,d\tau} \tag{6}$$

and leads to the exponential detection model

$$p(t) = 1 - q(t) = 1 - e^{-\int_0^t \gamma(\tau)\, d\tau}.$$

Equation (6) represents the probability that a target was not detected by time t, so the residual MCM risk after completing an operation of mission duration T_F is

$$q(T_F) = e^{-\int_0^{T_F} \gamma(\tau)\, d\tau} = e^{-\int_0^{T_F} \gamma(\vec{\mathbf{x}}(\tau), \vec{\boldsymbol{\omega}})\, d\tau}. \tag{7}$$

The objective of our optimal search problem is to minimize this risk. However, the instantaneous detection rate in (2) depends on the vehicle trajectory $\vec{\mathbf{x}}(t)$ and the uncertain target location $\vec{\boldsymbol{\omega}}$, a random variable defined in Section II-C. Consequently, (7) is itself a random variable, which cannot be explicitly minimized. Instead, we must minimize its expected value, conditioned on the pdf of the target distribution. Hence, the objective function for a single vehicle becomes

$$J = \mathbb{E}\left\{q(T_F)\right\} = \int_\Omega e^{-\int_0^{T_F} \gamma(\vec{\mathbf{x}}(\tau), \vec{\boldsymbol{\omega}})\, d\tau}\, \phi(\vec{\boldsymbol{\omega}})\, d\vec{\boldsymbol{\omega}}. \tag{8}$$

For missions with multiple search vehicles, we assume that the searchers make independent detection attempts as described in [53], each with an instantaneous detection rate that is vehicle and sensor specific. Using (7) and our independence assumption, the probability that all n_v searchers fail to detect a target during a multivehicle mission is

$$\begin{aligned} q^{n_v}(T_F) &= \prod_{k=1}^{n_v} e^{-\int_0^{T_F} \gamma^k\left(\vec{\mathbf{x}}^k(\tau), \vec{\boldsymbol{\omega}}\right) d\tau} \\ &= e^{-\int_0^{T_F} \sum_{k=1}^{n_v} \gamma^k\left(\vec{\mathbf{x}}^k(\tau), \vec{\boldsymbol{\omega}}\right) d\tau} = e^{-\int_0^{T_F} \Gamma(\tau, \vec{\boldsymbol{\omega}})\, d\tau} \end{aligned} \tag{9}$$

where we have

$$\begin{aligned} \Gamma(t, \vec{\boldsymbol{\omega}}) = \sum_{k=1}^{n_v} \gamma^k(\vec{\mathbf{x}}^k(t), \vec{\boldsymbol{\omega}}) = \sum_{k=1}^{n_v} \big\{ &\lambda^k\, p^k(\vec{\mathbf{x}}^k(t), \vec{\boldsymbol{\omega}}) \\ &\times\ F_\alpha^k(\vec{\mathbf{x}}^k(t), \vec{\boldsymbol{\omega}})\, F_\varepsilon^k(\vec{\mathbf{x}}^k(t), \vec{\boldsymbol{\omega}})\, F_r^k(\vec{\mathbf{x}}^k(t)) \big\}. \end{aligned} \tag{10}$$

Under our stated assumptions, the residual MCM risk after a multivehicle operation is

$$J^{n_v} = \mathbb{E}\left\{q^{n_v}(T_F)\right\} = \int_\Omega e^{-\int_0^{T_F} \Gamma(\tau, \vec{\boldsymbol{\omega}}) d\tau} \phi(\vec{\boldsymbol{\omega}})\, d\vec{\boldsymbol{\omega}}. \tag{11}$$

The independence assumption used to derive (9) also requires the implicit assumption that multiple sonars will not acoustically interfere with one another. The latter is usually only valid when individual sonar systems have widely separated design frequencies, or they have been assigned to different regions of the search area. As noted in Section I-A, it is common practice to divide larger search areas into smaller subregions that can be searched by a set of single-vehicle plans. By design, GenOC does not decompose multivehicle search problems into separate single-vehicle trajectories. Rather, its centralized planning approach can incorporate a variety of interaction models to facilitate collaboration or separation among vehicles [26]. On the other hand, GenOC users can simply impose constraints on minimum separation distance to generate plans that reduce potential for mutual acoustical interference. In any case, the exponential detection model used in our objective function often produces multivehicle search plans that resemble separate single-vehicle trajectories. Since it yields diminishing returns when multiple vehicles search the same location [21], it encourages multivehicle solutions that direct individual vehicles toward new regions of the search space.

Equations (8) and (11) comprise differentiable analytic expressions. Although somewhat tedious, it is possible to derive formulas for their gradients with respect to the state and control variables. This has benefits when using gradient-based numerical optimization algorithms. Encoding these formulas as user-defined functions supplied to the SNOPT optimization package, for example, significantly reduces the run time required to compute an optimal solution [54]. The objective function gradients for a single vehicle are derived in [55].

The objective functionals in (8) and (11) represent the expected residual MCM risk after a single- or multivehicle operation, respectively. They take the same form as the running cost in the Bolza-type cost functional for the GenOC problem described in [14]

$$\begin{aligned} J = \int_\Omega & E\left(\vec{\mathbf{x}}(T_f), \vec{\boldsymbol{\omega}}\right) \\ & + G\left(\int_0^{T_f} R(\vec{\mathbf{x}}(\tau), \vec{\mathbf{u}}(\tau), \tau, \vec{\boldsymbol{\omega}}) d\tau\right) \phi(\vec{\boldsymbol{\omega}})\, d\vec{\boldsymbol{\omega}}. \end{aligned} \tag{12}$$

For our problems, the endpoint cost $E(\vec{\mathbf{x}}(T_f), \vec{\boldsymbol{\omega}})$ has been omitted from the objective function in (12). Meanwhile, the function $G(\cdot)$ of the running cost derives from the exponential detection model, i.e., $G(\cdot) = e^{-(\cdot)}$, and $R(\cdot) = \gamma(\cdot)$. The objective functional in (12) has been used to solve optimal search problems with multiple searchers and moving targets in cases where target motion can be conditionally determined by uncertain initial conditions [14], [16], [56]. Using similar objective functions in (8) and (11) allows us to leverage the mathematical and computational framework previously developed to handle this class of parameter-distributed nonlinear optimal control problems.

E. Problem Scaling

We need to solve these optimal search problems numerically, but the domains of our state variables $\vec{\mathbf{x}}(t)$, control inputs $\vec{\mathbf{u}}(t)$, uncertain parameters $\vec{\boldsymbol{\omega}}$, and objective function J all have different orders of magnitude. The search area, for example, may cover several square kilometers, whereas the objective function evaluates to a probability in the range [0, 1]. It is important, therefore, to properly scale the problem before unleashing a numeric solver. This can be achieved by defining canonical units for distance, time, etc., and transforming the original problem's variables into nondimensional versions with similar domains [57]. Several examples that use variable scaling to numerically balance the equations of an optimal control problem are provided in [58]. For our search problems, the vehicle models from Section II-A can be scaled by canonical units of distance (DU), time (TU), and velocity (VU $=$ DU/TU) to produce dimensionless variables as shown in Appendix B. As an example, suppose we want to solve an MCM search problem for the *SeaFox* USV (see Section II-A1) conducting a mine detection survey with the 200-kHz FLS derived in Section III-E1. Typical bounds on the states, controls, search area, and constant parameters are defined in Table IV. This table includes their physical values (before scaling), and their nondimensional values after scaling by the canonical units DU $=$ 100 m, TU $=$ 100 s, and VU $=$ DU/TU $=$ 1 m/s.

F. Feasibility

Most optimal control problems cannot be solved analytically. Often, numerical methods are required to generate "optimal" trajectories of the state variables and control inputs that minimize a desired objective function, subject to constraints defined by the user. We must remember, however, that numeric solutions are calculated for a *discretized* version of the original problem. They meet the mathematical definition of feasibility as long as all of the problem constraints are satisfied at a finite number of nodes comprising the discrete problem [59]–[61]. It

TABLE IV
EXAMPLE OF PHYSICAL AND NONDIMENSIONAL PARAMETER DOMAINS

Parameter	Physical Domain		Canonical Domain
Time	$0 \leq t \leq 1800$	s	$0 \leq \bar{t} \leq 18$
Search Area Northing	$500 \leq \omega_x \leq 2500$	m	$5 \leq \overline{\omega}_x \leq 25$
Search Area Easting	$500 \leq \omega_y \leq 2500$	m	$5 \leq \overline{\omega}_y \leq 25$
Operating Area Northing	$0 \leq x \leq 3000$	m	$0 \leq \overline{x} \leq 30$
Operating Area Easting	$0 \leq y \leq 3000$	m	$0 \leq \overline{y} \leq 30$
Heading	$-\infty \leq \psi \leq \infty$	rad	$-\infty \leq \overline{\psi} \leq \infty$
Turn Rate	$-0.3 \leq r \leq 0.3$	rad/s	$-30 \leq \overline{r} \leq 30$
Rudder Angle Input	$-0.5 \leq u \leq 0.5$	rad	$-0.5 \leq \overline{u} \leq 0.5$
Velocity	$V = 2.5$	m/s	$\overline{V} = 2.5$
Nomoto Gain Const.	$K = 0.5$	1/s	$\overline{K} = 50$
Nomoto Time Const.	$T = 5.0$	s	$\overline{T} = 0.05$
Poisson Scan Rate	$\lambda = 0.2$	1/s	$\overline{\lambda} = 20$
Attenuation Coeff.	$a = 0.052$	dB/m	$\overline{a} = 5.2$

is important to verify that these constraints are, in fact, satisfied in the continuous domain as well. Moreover, we require optimal trajectories that can be implemented on autonomous vehicles. Therefore, as a practical consideration, we adopt the definition of feasibility used by Hurni:

> Showing the feasibility of the generated solution can be done by control trajectory interpolation and state propagation using a Runge–Kutta algorithm. If the initial conditions and system dynamics can be propagated using the optimal control solution and it matches the [solver's] generated trajectories, then the control solution is deemed feasible [58, p. 54].

In other words, solutions with discrete trajectories $\{\vec{\mathbf{x}}(k), \vec{\mathbf{u}}(k)\}$ are feasible if a vehicle can execute a smooth control trajectory $\vec{\mathbf{u}}(t)$, interpolated through the solution's $\vec{\mathbf{u}}(k)$ nodes, and produce a state trajectory $\vec{\mathbf{x}}(t)$ sufficiently close to the solution's $\vec{\mathbf{x}}(k)$ nodes. Planning algorithms can verify feasibility automatically, but the word "close" must be quantified first. Possible metrics for the similarity between two curves include the Frechet [62] or Hausdorff [63] distance measures. The trajectory planning algorithm proposed in [58], for example, performs automatic feasibility checks using a norm based on summing the Euclidean distances between the solution nodes and points along the propagated trajectory, evaluated at the solution nodes. In the following chapters, we will consider a solution to be feasible when its state-propagated trajectory does not violate problem constraints and matches the solution trajectory when overlaid on a graphical plot. These criteria will verify that solutions obtained from a numeric solver are feasible, and also ensure that only feasible guesses are used to initialize the optimization. When necessary, e.g., for the automated analysis of inverse problems conducted in [55], we employ a numeric feasibility criteria similar to [58].

G. Initial Guess

Most numeric optimization routines are initialized with an initial guess. For an optimal control problem, the guess is a candidate solution, complete with state and control trajectories $\{\vec{\mathbf{x}}(k), \vec{\mathbf{u}}(k)\}$ at discrete time nodes. The solver evaluates the objective function using these trajectories. From there, it iteratively generates new candidate solutions that decrease the objective value, finally stopping its search when it reaches a local minimum. A good initial guess can influence the optimization by focusing the solver's effort in smaller regions of the search space. As a result, initial guesses can dramatically reduce solution times [58]. In some cases, e.g., when a problem has several local minima, the initial guess can determine whether a solver succeeds or fails at finding the correct solution. Various methods used to generate initial guess trajectories for this article are described in Appendix C.

III. SONAR DETECTION MODELS

The SE model of sonar detection simulates the conditions under which an active or passive sonar system can detect an underwater object, based on well-known sonar equations. First proposed in [51], SE is still widely used in many sonar performance models today, including the U.S. Navy's Comprehensive Acoustic System Simulation (CASS), described in [64]–[66]. Due to complexity and computational runtime requirements, however, many performance models are unsuitable for sensor-based motion planning algorithms. Anecdotally, when CASS "is used as the acoustic calculation engine …computation of SE in support of a complex multistatic active sonar analysis task can take days" [67]. Our implementation, therefore, makes simplifying assumptions to rapidly compute SE for an active sonar attached to a moving vehicle platform as follows.

1) We assume that detection performance is limited only by acoustical background noise and neglect reverberation from backscattered acoustical energy, a complex function of time, range, and the environment (e.g., seabed roughness) [68]. The noise-limited form of the active sonar equation allows a constant FOM to be computed for each sonar design, enabling qualitative performance comparisons in a given environment.
2) We assume that the environment is homogeneous, with a flat bottom and constant water depth. We further assume a constant sound-speed profile, although sound speed varies as a function of temperature, salinity, and depth. These assumptions allow us to forgo computationally expensive ray tracing calculations.
3) We ignore multipath propagation effects, as MCM sonars typically operate at higher frequencies and relatively short ranges, e.g., hundreds of meters as opposed to tens of kilometers for a submarine sonar system.

The SE model assumes that detections can only occur when the acoustical energy transmitted by a sonar is sufficient to overcome the two-way PL in the environment, and the received signal reflected by a target exceeds a detection threshold (DT) relative to the prevailing background noise. This SE can be computed using well-known sonar equations, "simple algebraic expressions used to quantify various aspects of sonar performance" [22], with terms expressed in units of decibels (dB) relative to corresponding reference values [66]. For an active sonar operating against a noise background, and a DT expressed as a function of frequency modulated (FM) or continuous wave (CW) active pulse types, a typical SE equation from [68, p. 165] is

$$\mathrm{SE} = \mathrm{SL} - 2\mathrm{PL} + \mathrm{TS} - (N - \mathrm{DI} + 10\log_{10} B) - \mathrm{DT} \qquad (13)$$

where SE is the signal excess, SL is the source level, PL is the one-way PL, TS is target strength, N is omnidirectional sonar self-noise, DI is the directivity index, B is the pulse bandwidth in hertz, and DT is detection threshold.

DT can be computed as $\mathrm{DT} = 5\log_{10} d - 10\log_{10}(B\,T) - 5\log_{10} n$ for a detection index d, a pulse duration of T seconds, and n pings used to make detection decisions [68, p. 165]. The units for each term in (13) are dB unless otherwise specified. Section III-A uses this form of the sonar equation to derive the probabilistic sensor models at the heart of our motion planning algorithm.

The proposed sonar detection model introduces a number of additional parameters, which can be tuned to represent a particular sonar sensor. The task of precisely identifying parameter values, however, is outside the scope of this article for two primary reasons. On the one hand, we provide example models of prototype and commercial sonar systems (e.g., [69]–[71]) and include explicit relevant parameters used in the text. On the other hand, choosing an optimal value for a specific parameter is a problem that can be addressed by formulating an inverse problem as described in [55]. Namely, what are the optimal sonar parameters within the scope of an MCM mission, given the current limitations of a specific platform (vehicle type, sensor mount, etc.) that produce an optimal detection rate along a search trajectory? In other words, if a prototype sonar is provided as an initial guess, can we improve this sensor by optimally shaping its settings for improved mission performance? As such, Sections III-E and III-F provide parameter values that we have derived from comparable prototypes, obtained from manufacturer specifications, or discovered during our search for their optimal settings. The main objective is to present a tunable engineering model of sonar detection performance that balances sensitivity to vehicle motion, sensor configuration, etc. and computational simplicity needed for numeric optimization of MCM search trajectories.

A. Figure of Merit

For a sonar performance analysis, individual terms related to a specific sonar design are often combined into a FOM. For passive or noise-limited active sonars in a given scenario, this metric is constant and independent of range and environmental propagation characteristics. As a result, FOM permits direct comparison of different sonar models and greatly simplifies sonar performance calculations during trajectory optimization. We therefore restrict our analysis to the noise-limited case, since reverberation-limited performance prediction requires more sophisticated analysis tools [22]. Using FOM, the SE equation becomes

$$\mathrm{SE}(t) = \mathrm{FOM} - \mathrm{PL}\left(D(t)\right) \tag{14}$$

where $D(t)$ is the distance to the target in meters.

In this form, the one-way PL is a function of the distance between a stationary target and a search vehicle's location at time t, i.e., $D(t) = \|\vec{\boldsymbol{\omega}} - \vec{\mathbf{x}}(t)\|$. Recall that target location $\vec{\boldsymbol{\omega}}$ is uncertain but characterized by the pdf $\phi(\vec{\boldsymbol{\omega}}) : \boldsymbol{\Omega} \mapsto \mathbb{R}$. Physically, FOM represents the maximum allowable one-way PL resulting in zero SE. Assuming target detection is possible when $\mathrm{SE} \geq 0$, we compute FOM by substituting (13) into (14) when $\mathrm{SE} = 0$. Combining terms yields an expression for FOM as a function of the relevant design parameters [68, p. 165]

$$\begin{aligned} 0 = {} & \mathrm{SL} - 2\,\mathrm{FOM} + \mathrm{TS} - (N - \mathrm{DI} + 10\log_{10} B) \\ & - (5\log_{10} d - 10\log_{10}(B\,T) - 5\log_{10} n) \\ \mathrm{FOM} = {} & (\mathrm{SL} + \mathrm{TS} - N + \mathrm{DI} + 10\log_{10} T - 5\log_{10} d \\ & + 5\log_{10} n)/2. \end{aligned} \tag{15}$$

We briefly describe each of these parameters, and provide sample calculations for the values used in our simulations. Specific parameter values corresponding to models of individual sonar designs are derived in Sections III-E and III-F.

1) Source level (SL) of a projector array is a function of its acoustical power P. If the array is directional, SL also depends upon DI_t.
2) TS quantifies the intensity of a sound wave reflected by an underwater target relative to an incident sound wave from an active sonar pulse. This quantity is a function of sonar frequency, target size, geometry, and the angle of incidence between the sonar pulse and target. The goal of our MCM search problem is to detect small mines on the seafloor approximated by finite cylinders of radius 0.1 m and length 1.0 m, with hemispherical ends. For these targets, the worst case target strength (TS) occurs for sonar incident angles arriving parallel rather than normal to the cylinder axis. In this case, TS is computed for a sphere with radius a using the formula $\mathrm{TS} = 10\log_{10}(a^2/4) = -26$ dB [68, Table 4.1]. Therefore, our analysis uses the conservative value of $\mathrm{TS} = -30$ dB. We note, however, that augmenting the uncertain parameter space $\boldsymbol{\Omega}$ with target orientation θ_ω would allow optimal search plans to explicitly consider the aspect dependence of TS on searcher location and orientation. This remains an area of future investigation.
3) Noise *(N)* refers to the intensity level of the background noise that a desired signal must overcome to be detectable at the sonar receiver. The average spectral level for thermal noise usually dominates other noise sources at the high frequencies used for minehunting sonar, i.e., above 100 kHz, and can be computed for a given sonar frequency f in kilohertz using the expression in [72, p. 208]

$$N_{\text{therm}} = -15 + 20\log_{10} f \text{ dB}. \tag{16}$$

4) DI of a transducer array describes its ability to "concentrate transmitted sound in a given direction" (DI_t), and improve the signal-to-noise ratio (SNR) received from a given direction (DI_r) [68, p. 13]. This parameter is a function of the sonar's design frequency and array geometry.
5) Pulse duration *(T)* determines a sonar's range resolution, with shorter pulses providing better resolution due to smaller echo separation. A CW "pulse of constant frequency and duration T seconds" will have a bandwidth, $B = 1/T$ Hz. For FM pulses, "the frequency of the pulse changes during the T seconds duration of the pulse [and] the bandwidth B is *not* now the inverse of the pulse length" [68, p. 163].
6) Detection index *(d)* is used to determine a sonar receiving system's DT, expressed as the SNR corresponding to preset values for probability of detection (P_{D}) and probability of false alarm (P_{FA}). This relationship is typically plotted as a function of $5\log_{10} d$ on a curve of receiver operating characteristics. The sonar models derived below assume $5\log_{10} d = 10$ dB, corresponding to $P_{\mathrm{D}} = 0.5$ and $P_{\mathrm{FA}} = 10^{-5}$ as given in [68, Table 7.8].
7) The number of pings *(n)* contributing to a detection decision effectively reduces a sonar's DT as more information is considered. The models derived below assume $5\log_{10} n = 3$ dB, equivalent to processing four pings per decision [68].

Even though exact design parameters for Navy sonars are difficult to obtain (and potentially classified) [22], a FOM suitable for relative performance analysis can still be estimated from sonar design reference manuals [68] or commercial sonar specifications [69], [70], [73], [74]. Furthermore, once the FOM for a given sonar problem is known, it is easy to compute the SE along a moving vehicle's trajectory $\vec{\mathbf{x}}(t)$, since

it depends only on the PL due to distance between vehicle and target. Consequently, calculating detection probability based on signal excess is especially attractive for sensor-based motion planning algorithms.

B. Propagation Loss

An acoustical pulse loses intensity as it propagates through the water, as the radiated power spreads throughout a larger and larger volume. The pulse is also attenuated by absorption losses due to fluid viscosity and molecular relaxation of dissolved salts in seawater. Both spreading and absorption are functions of distance. For our signal excess calculations, we assume that PL are only due to spherical spreading and absorption, "a useful working rule for initial design and performance comparisons" [68, p. 48]. Neglecting other loss sources (e.g., scattering and refraction) via the simplifying assumptions listed in Section III, PL is

$$\mathrm{PL}(\vec{\mathbf{x}}(t), \vec{\boldsymbol{\omega}}) = 20 \log_{10} \left(\|\vec{\boldsymbol{\omega}} - \vec{\mathbf{x}}(t)\| \right) + a \, \|\vec{\boldsymbol{\omega}} - \vec{\mathbf{x}}(t)\| \qquad (17)$$

where a is the frequency-dependent attenuation coefficient of seawater. Tabulated values of a can be found in sonar design references, such as [68, Table 3.1] and [75]. While a varies with depth, salinity, and temperature, it depends most strongly on the sound frequency. We therefore compute this parameter as described in [72, p. 108], which estimates a as a function of frequency f in kilohertz

$$a = \frac{0.11 \, f^2}{1 + f^2} + \frac{44 \, f^2}{4100 + f^2} + 0.0003 \, f^2 + 0.003 \text{ dB/km}. \qquad (18)$$

C. Instantaneous Detection Rate

In search theory, "the detection rate approach to computation of detection probabilities has proved to be more robust than the geometric models" used by "cookie cutter" sensor models [21]. Originally developed in [51], this method assumes that a sensor has a detection rate $\gamma(t)$ called the "instantaneous probability density (of detection)." This rate may vary with time due to the motion of searchers and targets, or to reflect changing environmental conditions, for example. Continuously searching over a small time interval Δt constitutes a single glimpse or scan with the sensor. Each glimpse provides a detection opportunity with the instantaneous probability of detecting a target given by $\gamma(t) \, \Delta t$. This leads to the well-known exponential detection model described in Section II-D, which quantifies detection probability as a function of time.

Before we use this detection model, we must first compute detection rates for our sonar models. Detection rates based on our noise-limited SE model vary with distance between a target location $\vec{\boldsymbol{\omega}}$ and a search vehicle following the trajectory $\vec{\mathbf{x}}(t)$. If we also assume that the SE in (14) is a normally distributed random variable with mean SE and variance σ^2, the instantaneous probability of detection for a single glimpse with a sonar can be written using its cumulative normal distribution Φ in [21, eq. (3.2-1)]

$$p(\vec{\mathbf{x}}(t), \vec{\boldsymbol{\omega}}) = \Phi \left(\mathrm{SE} \left(\vec{\mathbf{x}}(t), \vec{\boldsymbol{\omega}} \right) / \sigma \right). \qquad (19)$$

Based on our selection of the detection index d in Section III-A, the instantaneous detection probability is $p(t) = 0.5$ when $\mathrm{SE}(t) = 0$, meaning the sonar has an equal probability of detecting or missing a mine. Regarding the selection of σ, Washburn notes that "most practitioners use a value of σ somewhere between 3 and 9 dB for sonar detection in the ocean" [21, Ch. 3, p. 2]. A value of $\sigma = 5.6$, computed by adding typical variance values for each term in the sonar equation, is provided in [22]. Moreover, a study which used the Navy's CASS/Gaussian Ray Bundle software to simulate mine detections under varying environmental conditions observed SE variations of 3, 6, or 9 dB in most cases [76], [77]. Fig. 7 plots probability of detection P_{D} versus SE for these three values of σ. To compute a sonar's detection rate $\gamma(t)$ from its instantaneous detection probability $p(t)$, we further assume that detection opportunities (glimpses) can be modeled as a Poisson process and occur with mean rate λ. The so-called Poisson scan model produces the detection rate $\gamma(\vec{\mathbf{x}}(t), \vec{\boldsymbol{\omega}}) = \lambda \, p(\vec{\mathbf{x}}(t), \vec{\boldsymbol{\omega}})$ [21, Ch. 3, p. 2].

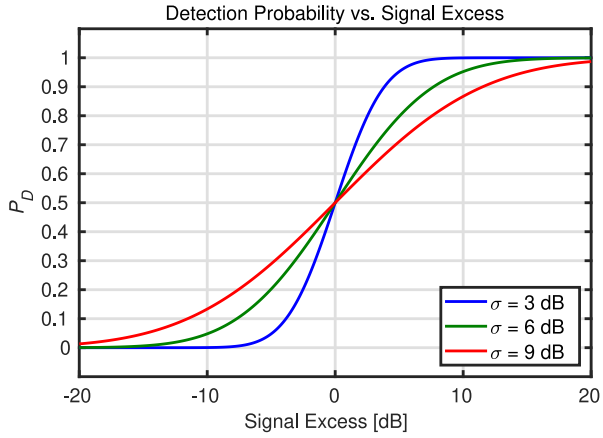

Fig. 7. Detection probability P_D versus SE for different values of σ.

D. Detection Performance Modifiers

The sonar detection model developed thus far, based on SE remaining after subtracting PL from a given sonar's figure of merit, is omnidirectional. It depends only on the distance between the sonar and a MLO. This function could be used to construct a lateral range curve and corresponding sweep width for use in standard coverage planning algorithms [2]. Most actual sonar systems, however, are designed to transmit and receive with a specific beam pattern (see, e.g., Figs. 2 and 3) and do not perform equally well in all directions. Actual detection performance depends not only on a sonar's distance from a target, but also whether (and how long) it is pointed in the proper direction, at the proper time and place, to ensonify the target. The vehicle platform must maneuver to accomplish this. Conversely, high-resolution imaging sonars, which rely on platform motion to methodically scan the seafloor (e.g., SSS) or construct long virtual hydrophone arrays [e.g., synthetic aperture sonar (SAS)], require precise navigation along straight line trajectories to generate accurate imagery [4], [78]. Excessive platform motion can often yield poor performance for these systems. It is clear that sonar performance is tightly coupled to a vehicle's motion. Section III-D-1 derives tunable shaping functions to model a sonar's 3-D beam geometry, while Section III-D-2 derives a shaping function to model its dependence on platform motion.

It should be noted that mission-level search performance also depends upon the navigation accuracy of the search vehicle, i.e., the ability of the searcher to follow prescribed trajectories generated by its motion planner. Pollitt's review of tactical decision aids (TDAs) developed for MCM since the Vietnam War remarks how "MCM operations require close adherence to sweep or hunt tracks, as percent clearance is degraded when the navigation error increases" [79]. The author also refers to a tactical memorandum released in 1991 by Commander, Mine Warfare Command that described "the relationship between navigational error and MCM effectiveness" [79]. Current mine warfare doctrine still states that "critical to the success of route survey operations is the availability of a precise navigation system of a common type for all MCM assets," but "the consistency of the GPS and the

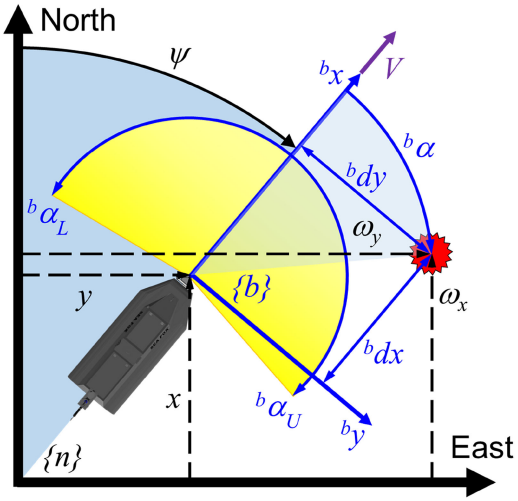

Fig. 8. Horizontal plane geometry for a USV with FLS.

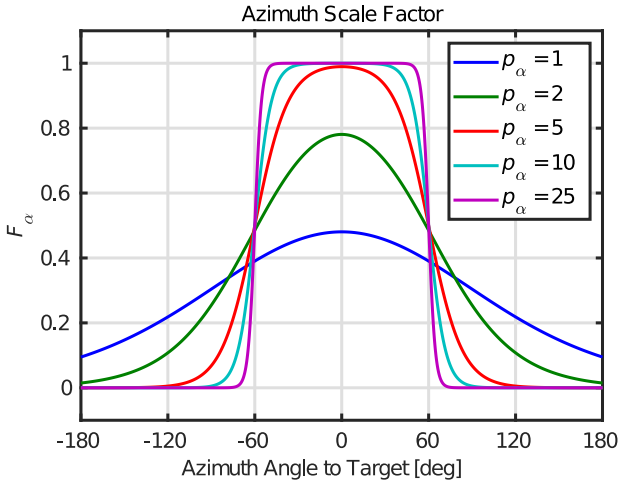

Fig. 9. F_α versus azimuth angle and p_α for a nominal FLS with 120° horizontal FOV.

precise navigation and plotting systems now available" allow MCM units to "hunt or sweep a track" and relocate contacts with confidence [80]. For this reason, and because our GenOC formulation generates *feasible* search trajectories that a vehicle's autopilot can follow, we exclude the vehicle's positioning system in the following models of detection performance.

1) FOV Considerations: To more accurately estimate a sonar's true detection performance when mounted on a vehicle, we must enforce its actual beam geometry in 3-D. First, we define angular limits for the sonar's horizontal and vertical FOV. These FOV boundaries exist in the sonar reference frame, but we will assume without loss of generality that this frame is identical to the vehicle's body-fixed reference frame. Next, we calculate the vectors between the sonar and each potential target, and resolve them in the body-fixed reference frame to compute the angle to each target relative to the sonar's field of view (FOV). Finally, we apply a shaping function to degrade detection performance for targets that fall outside of the angular FOV limits.

Fig. 8 depicts the instantaneous horizontal plane geometry for a *SeaFox* USV and FLS with horizontal FOV, α_{FOV}, of 200°. Parameters defined or resolved in the body-fixed frame $\{b\}$ are denoted with a superscript b. The positions of the USV $[x, y]^\top$ and potential mine target locations $[\omega_x, \omega_y]^\top$ are defined in the inertial reference frame $\{n\}$. We compute the lower and upper limits on azimuth angle for a sonar's horizontal FOV by the expressions ${}^b\alpha_L = -\alpha_{\text{FOV}}/2$ and ${}^b\alpha_U = +\alpha_{\text{FOV}}/2$, respectively.

The vector between the sonar and a target of interest in the inertial frame is then defined as $\Delta\vec{\mathbf{x}} = [\omega_x - x,\ \omega_y - y]^\top = [dx,\ dy]^\top$. To determine the azimuth angle to this target in the sonar's FOV, the vector $\Delta\vec{\mathbf{x}}$ must be resolved in the body-fixed reference frame using the vehicle's heading angle ψ, producing the body-fixed components as

$$ {}^b dx = \ {}^n dx \cos\psi \ + \ {}^n dy \sin\psi \tag{20}$$

$$ {}^b dy = -{}^n dx \sin\psi \ + \ {}^n dy \cos\psi. \tag{21}$$

Then, using the four-quadrant inverse tangent, we compute ${}^b\alpha = \text{atan2}({}^b dy,\ {}^b dx)$. In the same manner, we compute the lower and upper limits on elevation angle for the sonar's vertical FOV as ${}^b\varepsilon_L = \varepsilon_{\text{DE}} - \varepsilon_{\text{FOV}}/2$ and ${}^b\varepsilon_U = \varepsilon_{\text{DE}} + \varepsilon_{\text{FOV}}/2$, respectively. Here, ε_{DE} is a fixed downward elevation angle selected to ensure that the sonar can ensonify the seafloor. Some sonar systems are capable of electronically steering their beams to a specified ε_{DE}, but this angle is frequently determined by a fixed mechanical mounting angle. For a vehicle traveling in the horizontal plane at constant altitude h above the bottom, the elevation angle between the sonar and a mine on the seafloor is identical in both reference frames

$$\begin{aligned} \varepsilon = \ {}^b\varepsilon = \ {}^n\varepsilon &= \arctan\left(\frac{-h}{\sqrt{(\omega_x - x)^2 + (\omega_y - y)^2}}\right) \\ &= \arctan\left(\frac{-h}{\sqrt{dx^2 + dy^2}}\right). \end{aligned} \tag{22}$$

We now define scalar shaping functions, which degrade sonar detection performance for mines outside the sonar's horizontal (or vertical) FOV. Each shaping function is constructed from two logistic functions [81]. These S-shaped sigmoidal curves [82] smoothly transition a scalar value from 0 to 1 at the angular limits of the sonar's FOV. This value modifies the probability of detecting mines based on SE alone, thereby preventing detection of mines located outside these angular limits. As discussed in Section III-D3, parameters p_α and p_ε are used to adjust the slope of the sigmoidal curves in the azimuth and elevation shaping functions, respectively, as follows:

$$\begin{aligned} F_\alpha(\vec{\mathbf{x}}(t), \vec{\boldsymbol{\omega}}) = &\frac{1}{1 + e^{p_\alpha\left({}^b\alpha_L - {}^b\alpha(\vec{\mathbf{x}}(t), \vec{\boldsymbol{\omega}})\right)}} \\ &+ \frac{1}{1 + e^{p_\alpha\left({}^b\alpha(\vec{\mathbf{x}}(t), \vec{\boldsymbol{\omega}}) - {}^b\alpha_U\right)}} - 1 \end{aligned} \tag{23}$$

$$\begin{aligned} F_\varepsilon(\vec{\mathbf{x}}(t), \vec{\boldsymbol{\omega}}) = &\frac{1}{1 + e^{p_\varepsilon\left({}^b\varepsilon_L - {}^b\varepsilon(\vec{\mathbf{x}}(t), \vec{\boldsymbol{\omega}})\right)}} \\ &+ \frac{1}{1 + e^{p_\varepsilon\left({}^b\varepsilon(\vec{\mathbf{x}}(t), \vec{\boldsymbol{\omega}}) - {}^b\varepsilon_U\right)}} - 1. \end{aligned} \tag{24}$$

Fig. 9 plots the azimuth scale factor versus target azimuth angle and several values of p_α for a nominal FLS with a 120° horizontal FOV. Similarly, Fig. 10 plots the elevation scale factor versus target elevation angle and several values of p_ε for a nominal FLS with a 30° vertical FOV mounted at $\varepsilon_{\text{DE}} = -15°$. Although the x-axes of Figs. 9 and 10 show azimuth (or elevation) angles in degrees, both functions are actually computed for angles in radians.

The plots in Figs. 11 and 12 illustrate how detection probability based on SE can be shaped using a sonar's FOV. The color map indicates the probability of detecting a mine relative to the sonar's reference

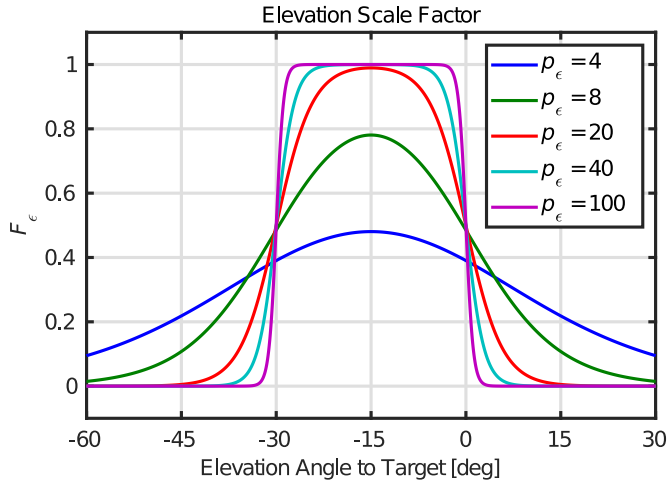

Fig. 10. F_ε versus elevation angle and p_ε for a nominal FLS with 30° vertical FOV mounted at −15°.

frame. Fig. 11(a) shows the omnidirectional detection probability in the horizontal plane, based on SE, for a FLS with FOM = 72 dB and $\sigma = 9$ dB. Fig. 11(b) shows the modified detection probability after applying an azimuth scale factor F_α corresponding to a horizontal FOV of 120° with $p_\alpha = 10$. Similarly, Fig. 12(a) shows the modified detection probability in the vertical plane after applying an elevation scale factor F_ε for a vertical FOV of 30° with $p_\varepsilon = 40$. The sonar head is mounted on a surface craft with $\varepsilon_{\text{DE}} = -15°$. Note that the different scales used for distance (x-axis) and depth (z-axis) distort the apparent beam angle in this plot, but the closeup view in Fig. 12(b), plotted with equal axis scaling, reflects the expected vertical FOV.

For an SSS comprised of dedicated port and starboard arrays, it is still possible to construct a continuous shaping function that describes both fields of view over the entire range of azimuth angles ${}^b\alpha \in [-\pi, \pi]$. In this case, we define the lower and upper azimuth limits as ${}^b\alpha_L = \alpha_{\text{mid}} - \alpha_{\text{FOV}}/2$ and ${}^b\alpha_U = \alpha_{\text{mid}} + \alpha_{\text{FOV}}/2$, respectively, relative to the center of the starboard array's FOV (i.e., $\alpha_{\text{mid}} = \pi/2$). The shaping function for the starboard array is calculated as before, i.e.,

$$ {}^{\text{stbd}}F_\alpha(\vec{\mathbf{x}}(t), \vec{\boldsymbol{\omega}}) = {}^{\text{FLS}}F_\alpha(\vec{\mathbf{x}}(t), \vec{\boldsymbol{\omega}}) $$

using (23) and these new angular limits. Next, the shaping function for the port side array is calculated as

$$ {}^{\text{port}}F_\alpha(\vec{\mathbf{x}}(t), \vec{\boldsymbol{\omega}}) = \frac{1}{1 + e^{-p_\alpha\left({}^b\alpha_L + {}^b\alpha(\vec{\mathbf{x}}(t), \vec{\boldsymbol{\omega}})\right)}} + \frac{1}{1 + e^{p_\alpha\left({}^b\alpha(\vec{\mathbf{x}}(t), \vec{\boldsymbol{\omega}}) + {}^b\alpha_U\right)}} - 1. \quad (25) $$

Combining these shaping functions yields

$$ {}^{\text{SSS}}F_\alpha(\vec{\mathbf{x}}(t), \vec{\boldsymbol{\omega}}) = {}^{\text{stbd}}F_\alpha(\vec{\mathbf{x}}(t), \vec{\boldsymbol{\omega}}) - {}^{\text{port}}F_\alpha(\vec{\mathbf{x}}(t), \vec{\boldsymbol{\omega}}). \quad (26) $$

Fig. 13 plots the azimuth scale factor versus target azimuth angle and several values of p_α for a nominal SSS with a 10° horizontal FOV. We now combine the effects of SE, three-dimensional FOV geometry, and average Poisson Scan rate of a given sonar to compute the modified instantaneous detection rate

$$ \gamma(\vec{\mathbf{x}}(t), \vec{\boldsymbol{\omega}}) = \lambda\, p(\vec{\mathbf{x}}(t), \vec{\boldsymbol{\omega}})\, F_\alpha(\vec{\mathbf{x}}(t), \vec{\boldsymbol{\omega}})\, F_\varepsilon(\vec{\mathbf{x}}(t), \vec{\boldsymbol{\omega}}). $$

2) Turn Rate Considerations: Recall that some types of sonar require stable straight line motion by its vehicle platform to produce high-resolution imagery. SSS, for example, stacks the backscattered signals received from successive pings to produce an image of the

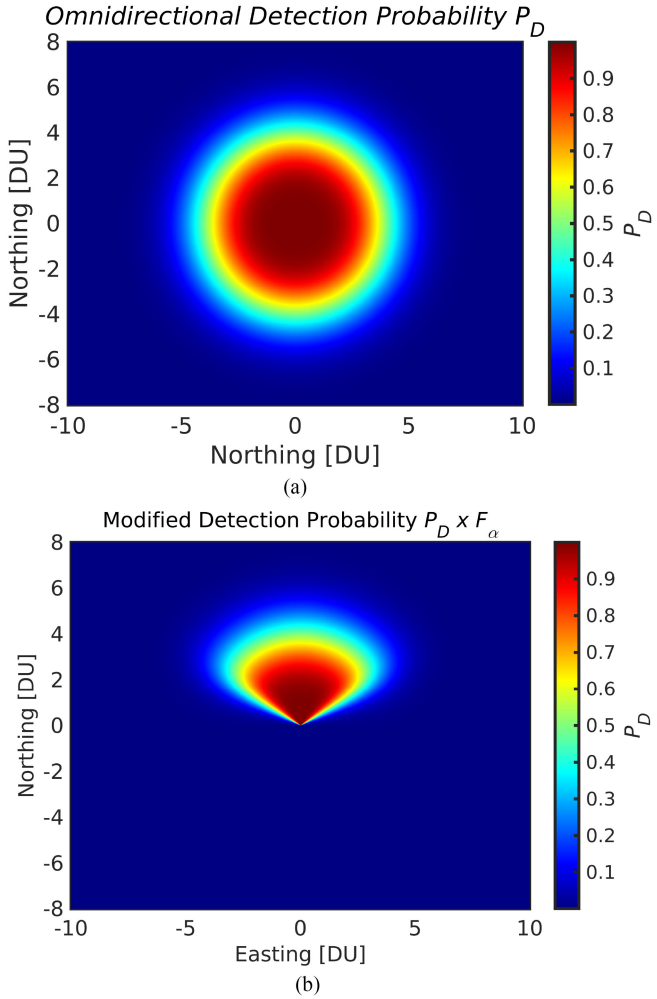

Fig. 11. Horizontal plane detection probability versus relative target location. (a) Omnidirectional. (b) Modified by F_α for 120° horizontal FOV.

seafloor. The across-track dimension of the resulting image corresponds to the two-way travel time of each ping, while the along-track dimension is formed by the vehicle's forward motion. Turning maneuvers, therefore, have a direct impact on SSS performance [83]. In fact, "yawing motions …are considered to have potentially the most serious degrading effects on sidescan images, because yaw causes the beam footprint to move along-track a distance proportional to the distance across-track" [84]. We model this behavior by applying another scale factor to degrade detection probability as a function of the vehicle turn rate $r(t)$. We select the Gaussian-like expression

$$ F_r(\vec{\mathbf{x}}(t)) = e^{-[r(t)/\sigma_r]^2/2}. \quad (27) $$

This function reaches a maximum value of one for straight line motion, e.g., when $r(t) = 0$, but falls off smoothly for nonzero turn rates. The slope of this curve can be adjusted via the tuning parameter σ_r, as shown in Fig. 14. Applying this scale factor, we obtain (2) for the instantaneous detection rate

$$ \gamma(\vec{\mathbf{x}}(t), \vec{\boldsymbol{\omega}}) = \lambda\, p(\vec{\mathbf{x}}(t), \vec{\boldsymbol{\omega}})\, F_\alpha(\vec{\mathbf{x}}(t), \vec{\boldsymbol{\omega}})\, F_\varepsilon(\vec{\mathbf{x}}(t), \vec{\boldsymbol{\omega}})\, F_r(\vec{\mathbf{x}}(t)). $$

3) Numeric Considerations: A primary consideration when selecting the shaping functions described in Sections III-D1 and III-D2 is their numerical smoothness. We shall see how instantaneous detection rate can be used to create an objective function for our optimal search

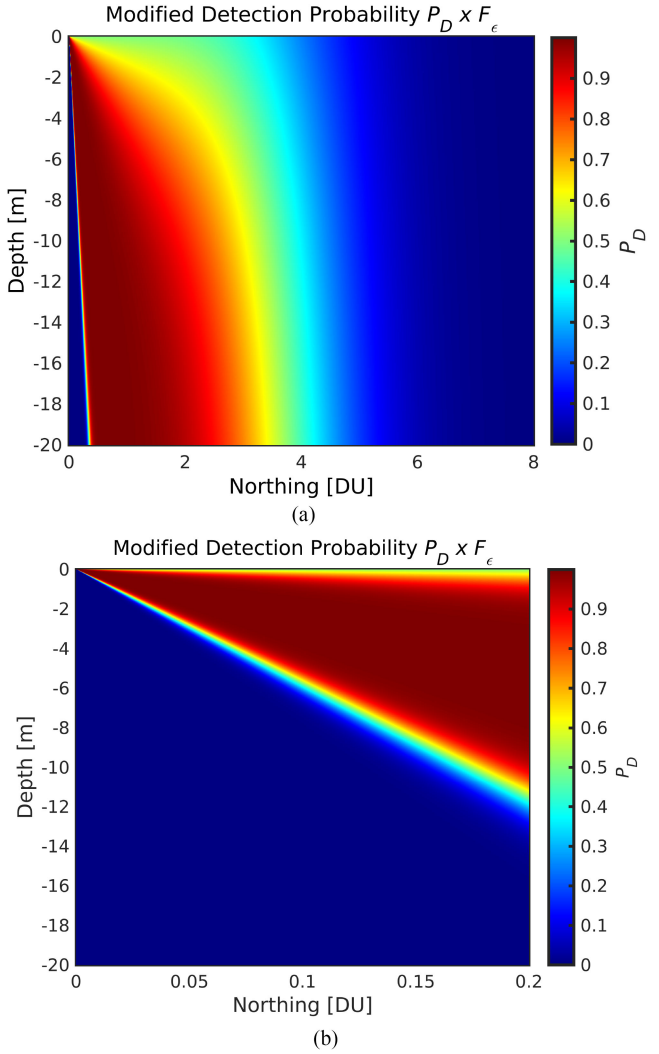

Fig. 12. Vertical plane detection probability versus relative target location, modified by F_ε for 30° vertical FOV mounted at $\varepsilon_{\text{DE}} = -15°$. (a) Full range view. (b) Closeup view.

problem. Having a smooth (i.e., differentiable) objective function is extremely helpful when performing numeric optimization. Another consideration is the ability to derive and encode analytic expressions for the objective function gradients. The SNOPT software package used to solve our optimal search problem, for example, "is able to estimate gradients by finite differences …for each variable whose partial derivatives need to be estimated. However, this reduces the reliability of the optimization algorithms, and it can be very [computationally] expensive if there are many such variables" [54].

These shaping functions were also designed to be flexible, as the logistic functions can be calibrated to reflect most sonar FOV geometries by setting the azimuth/elevation angular limits and growth parameters. Tuning the growth parameter p_α for azimuth angle in (23), or tuning p_ε for elevation angle in (24) will control the slope of a sonar's respective FOV boundary between regions of high and low detection probability. Low parameter values result in a gradual transition. As values increase, however, this transition tends toward a discontinuous step function, which presents numerical difficulties. Therefore, we have derived a heuristic for selecting appropriate growth parameter values based on the following two qualitative metrics:

TABLE V
DETECTION PERFORMANCE MODIFIERS USED IN NUMERICAL SIMULATIONS

Detection Performance Modifier	Forward-Looking Sonar			Sidescan Sonar
	Cylindrical Array	Blazed Array		
	200 kHz	450 kHz	900 kHz	900 kHz
α_{FOV}	120°	90°	90°	3°
p_α	17	22	22	125
ε_{FOV}	5°	10°	20°	40°
ε_{DE}	−6°	−7°	−11°	−10°
p_ε	400	200	100	85
σ_r	—	—	—	0.3°/s

1) scale factor threshold (SFT), the value the scale factor should attain within the sonar's FOV;
2) fraction below threshold (FBT), the portion of the nominal FOV below the desired SFT.

The logistic function, evaluated at the boundary of a sonar's horizontal or vertical FOV, can be rearranged to calculate growth parameter values that satisfy these metrics. These expressions become

$$p_\alpha = -2\ln(1 - \text{SFT})/[(\text{FBT})(\text{FOV}_{\text{hor}})]$$

and

$$p_\varepsilon = -2\ln(1 - \text{SFT})/[(\text{FBT})(\text{FOV}_{\text{ver}})]$$

for use in the azimuth and elevation shaping functions, respectively. One can experiment with these metrics to arrive at growth rate values that strike a balance between realistic FOV boundaries and objective function smoothness during numeric optimization. The values of p_α and p_ε used for the numerical studies of Sections IV and V are listed in Table V. These values were selected from a range of values for which simulated model performance agreed with nominal sonar specifications. Finally, we acknowledge that for distances less than 1 m, the spherical spreading term $20\log_{10}(\|\vec{\omega} - \vec{\mathbf{x}}(t)\|)$ in (17) will contribute a negative PL, since spreading losses are defined relative to an intensity measured 1 m from the source. Even more concerning is the fact that this term is undefined when the distance equals zero. Since our MCM problem is searching for bottom mines, however, the distance to any mine target is guaranteed to exceed 1 m as long as the search vehicle altitude exceeds 1 m above the seafloor.

E. FLS Models

This section derives FOM values for the FLS models used in this article. We consider the following two different designs.

1) A long-range low-resolution sonar designed with a cylindrical transducer array to provide a wide horizontal FOV. This type of sonar is typically used for wide area surveys to detect MLOs during the first phase of an MCM operation.
2) High-resolution blazed array imaging sonar suitable for RID of previously detected targets during follow-on MCM missions.

Both FLS designs are examples of "sectorscan sonar," which generate 2-D images from each pulse [78]. Examples of this imagery are shown in Figs. 15 and 16.

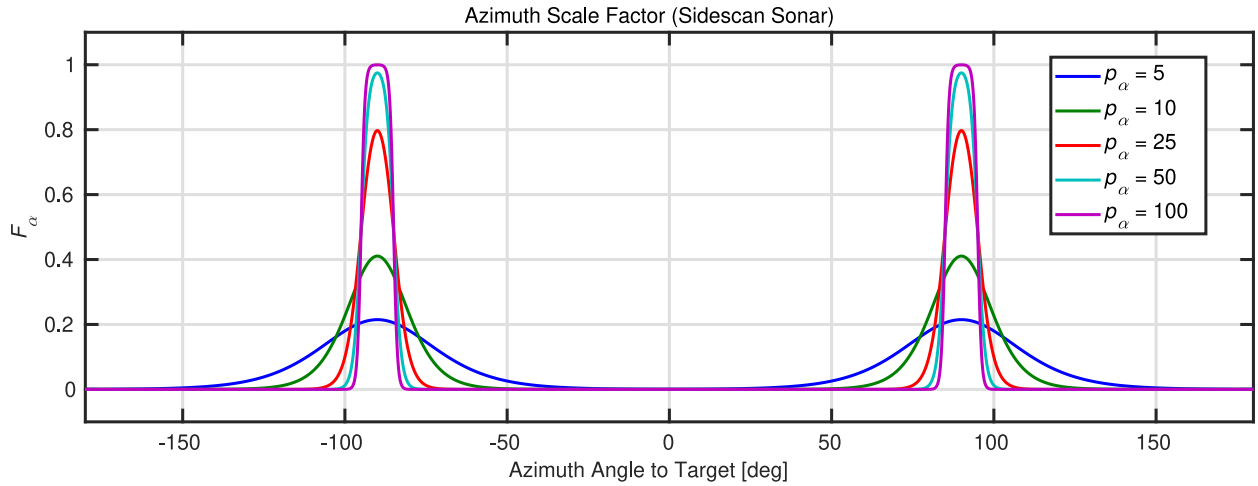

Fig. 13. F_α versus azimuth angle and p_α for a nominal SSS with 10° horizontal FOV.

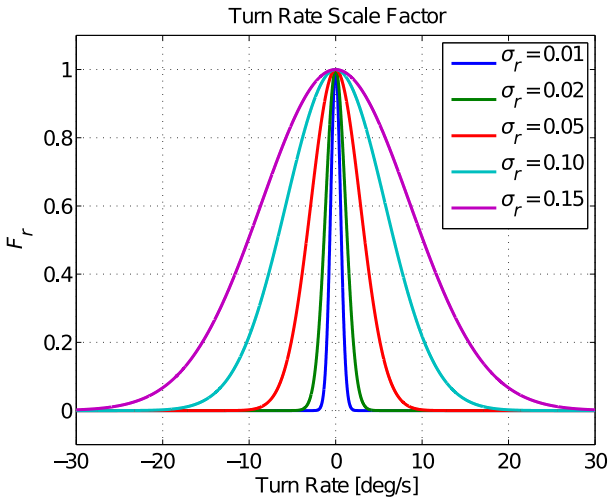

Fig. 14. F_r versus turn rate $r(t)$ and σ_r for a nominal SSS.

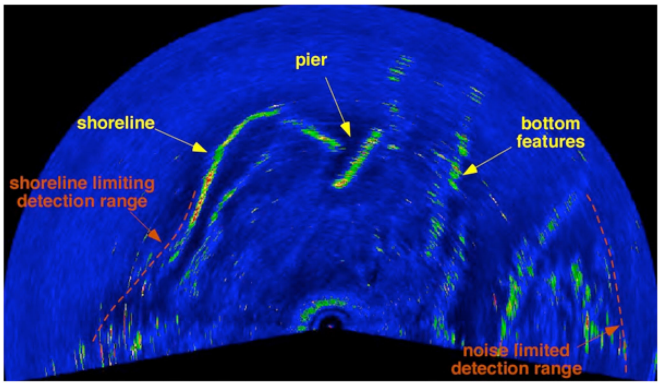

Fig. 15. Sample image from an ATLAS cylindrical array FLS. Image courtesy of Thunder Bay 2010 Expedition, NOAA-OER. Source: [85].

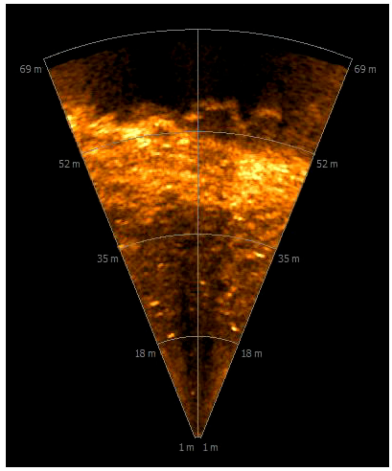

Fig. 16. Sample image from a BlueView P450 blazed array FLS.

Fig. 17. ATLAS FLS mounted on the NPS *SeaFox* USV.

1) Cylindrical Array Model: A cylindrical array of transducer elements is a common and practical sonar design. Individual elements are grouped into vertical lines, or staves, to obtain a desired vertical beamwidth, and multiple staves are arranged into a ring to provide the required azimuth coverage [68, p. 34]. Arrays of this type can be found on submarines (e.g., in [77] and [86]), and in systems, such as the ATLAS, shown mounted on the NPS *SeaFox* USV in Fig. 17. A FOM for a long-range detection sonar similar to ATLAS can be computed using the design example for a minehunting sonar described in [68, Ch. 11].

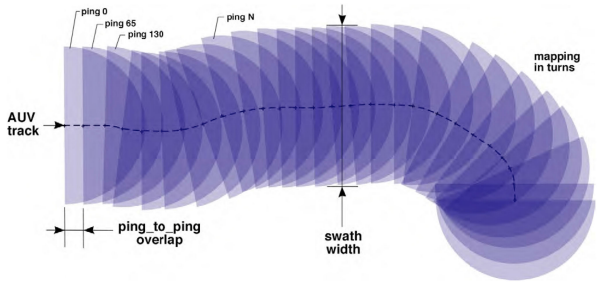

Fig. 18. Ping-to-ping overlap for a wide sector FLS. Image courtesy of Thunder Bay 2010 Expedition, NOAA-OER. Source: [85].

We specify a 200-kHz sonar with 120° horizontal FOV, 5° vertical FOV, and a nominal operating range of 400 m. We assume that this sonar transmits an FM pulse with bandwidth $B = 80$ kHz and duration $T = 10$ ms, which yields better noise-limited performance than a CW pulse for the values used in [68, p. 239]. We further assume that the sonar's projector array comprises multiple transducer elements so it can steer its beam in the vertical plane. From [68, Table 2.3] the number of elements required for a sonar stave to achieve a beamwidth BW of 5° is $n = 100/\mathrm{BW} = 100/5 = 20$. Assuming that the horizontal transmit beamwidth is 120°, the projector array requires only $m = 1$ vertical stave, and the transmit directivity index (DI) for this baffled cylindrical array can be calculated from [68, Table 2.5] by the expression $\mathrm{DI}_t = 3 + 10\log_{10}(m\,n) = 3 + 10\log_{10}(20) = 16$ dB. If we assume that the total acoustical power radiated by this projector is $P = 10$ W, we compute the SL for the sonar as described in [68, p. 4]

$$\mathrm{SL} = 10\log_{10} P + 170.8 + \mathrm{DI}_t = 197 \text{ dB}. \tag{28}$$

Turning attention to the sonar's receive array, we specify narrow 2° horizontal and vertical beamwidths so the sonar can resolve small MLOs in its FOV. Waite provided a formula for calculating the receive DI of a baffled cylindrical array based on its height h in meters, diameter d in meters, and design frequency f in kHz [68, Table 2.5]. For this sonar, the receive DI is

$$\mathrm{DI}_r = 10\log_{10}(5\,h\,d\,f^2). \tag{29}$$

Assuming half-wavelength spacing of its transducer elements (a function of the design frequency), the array's height $h = 76/(\mathrm{BW}_{\mathrm{ver}} \times f) = 76/(2 \times 200) = 0.19$ m, whereas its diameter $d = 88/(\mathrm{BW}_{\mathrm{hor}} \times f) = 88/(2 \times 200) = 0.22$ m [68, p. 35]. Substituting these values into (29), we compute $\mathrm{DI}_r = 39$ dB for this receive array.

Next, we compute the attenuation coefficient using (18), and the noise background due to thermal agitation using (16), both functions of the sonar's 200-kHz design frequency. The attenuation coefficient is $a = 52$ dB/km and the noise due to thermal agitation is $N_{\mathrm{therm}} = 31$ dB. However, we use a more conservative value of $N = 34$ dB to compute FOM in (15). This 3-dB increase can accommodate additional self-noise from the vehicle platform at levels comparable to the calculated N_{therm} value, e.g., for loud vehicles, such as the NPS *SeaFox* USV.

Finally, we estimate the Poisson Scan rate for this sonar model using the concept of "ping-to-ping overlap" illustrated in Fig. 18. This capability generates multiple looks, from different viewpoints, at MLOs on the seafloor, providing better detection and mapping performance [85]. It also makes sector scan sonar more robust to turning maneuvers than SSS, provided the vehicle platform has sufficiently accurate navigation. To ensure 95% ping-to-ping overlap from a sonar with 400-m swath width, mounted on an AUV traveling 1.5 m/s, the sonar must ping about every 10 s. Therefore, To accommodate faster USV platforms, we assume that our sonar model pings every 5 s, which corresponds to a Poisson Scan rate $\lambda = 0.2$ scans per second.

The parameters used to model this sonar are listed in Table VI. All specified (or assumed) values are *italicicized*, whereas calculated values are listed in plain text. The operating frequency, projector SL, cylindrical array geometry, and pulse characteristics chosen for this design yield a FOM of 72 dB.

2) Blazed Array Models: A relatively recent sonar design technique, based on "blazed" arrays, has led to a class of smaller, lighter, and lower power imaging sonars, which are well suited for deployment from small AUVs. Leveraging techniques from the fields of radar and optics, a blazed array can "map angular image information into the frequency domain" [87]. In principle, these acoustical arrays are analogous to optical diffraction gratings, which can separate a broad spectrum signal (white light) into individual and angularly separated frequencies (colors) [88]. Blazed sonar arrays separate a broadband acoustical pulse into a "frequency-dispersed sound field" in which each frequency corresponds to a separate sonar beam. Unlike traditional sonar designs that use dedicated electronics to form and steer the beams generated by each stave in the array, e.g., [89], "this approach allows multiple independent beams to be simultaneously formed from a single hardware channel" [87].

In this section, we apply the procedure described in Section III-E1 to compute FOM values for two blazed array multibeam imaging sonars. Teledyne BlueView's P450 Series and P900 Series systems are modular designs comprised of multiple blazed arrays that operate at 450 and 900 kHz center frequencies, respectively. Fig. 19 illustrates how individual staves can be combined to form a larger FOV. We will model the P450-90 and P900-90 sonars, which utilize four staves to produce a 90° horizontal FOV.

An individual stave produces a 25° fan of beams in the image plane, each with a distinct frequency and angle relative to the face of the stave. The lowest frequency beam angle is 45°, and the highest frequency beam angle is 70°, as shown in Fig. 19(a). The combined 3-D FOV for a two-stave system is depicted in Fig. 19(b), illustrating how the beamwidths vary with frequency in both the image- and cross-image planes. Although beam pattern geometries for multiple stave systems, such as those depicted in [90], are complex, we assume that image processing algorithms allow us to model these sonars as conventional line arrays operating at the center frequency of their broadband pulse. Under this assumption, manufacturer specifications can be used for operating frequency, FOV, beamwidth (in the image- and cross-image planes), number of beams, and update rate to calculate a FOM for the P450-90 [69] and P900-90 sonars [70]. We further assume that these sonars use an FM pulse duration $T = 10$ ms.

Note that the manufacturer's specifications list the total number of beams in a given sonar. Since these sonars are constructed using modular staves, each with 128 individual beams, we compute the DI for a single stave using the expression from [68, Table 2.5] for a baffled line array with $n = 128$ elements. For this sonar, the DI is

$$\mathrm{DI}_t = \mathrm{DI}_r = 3 + 10\log_{10} n = 3 + 10\log_{10}(128) = 24 \text{ dB}. \tag{30}$$

The transmit SLs for the P450-130 and P900-45 sonars are given in [91] as 207 and 206 dB, respectively. Using (28) and the calculated value for $\mathrm{DI}_t = 24$ dB, the total acoustical power level P is between 13 and 17 W, a reasonable result given that the stated electrical power consumption for these models is between 15 and 30 W.

Next, we use (18) to compute attenuation coefficients for the 450 and 900 kHz operating frequencies of $a = 104$ dB/km and $a = 287$ dB/km, respectively. From (16), we estimate that the noise due to thermal agitation are $N_{\mathrm{therm}} = 38$ dB and $N_{\mathrm{therm}} = 44$ dB, respectively. After accommodating additional self noise from the vehicle platform (which

TABLE VI
SONAR DESIGN PARAMETERS USED TO CALCULATE NOISE-LIMITED FOM

	Sonar Design Parameters	Forward-Looking Sonar			Sidescan
		Cylindrical Array	Blazed Array		Sonar
Specified or Assumed	*Frequency*	200 kHz	450 kHz	900 kHz	900 kHz
	Nominal Range	400 m	200 m	100 m	40 m
	Transmit Beamwidths				
	Horizontal	120°	90°	90°	0.4°
	Vertical	5°	10°	20°	40°
	Receive Beamwidths				
	Horizontal	2°	1°	1°	0.4°
	Vertical	2°	10°	20°	40°
	Pulse Length, T				
	FM Pulse	10 ms	10 ms	10 ms	—
	CW Pulse	—	—	—	6.67 μs
	Pulse Bandwidth, B				
	FM Pulse	80 kHz	80 kHz	80 kHz	—
	CW Pulse	—	—	—	150 kHz
	Detection Index, $5\log_{10} d$	10 dB	10 dB	10 dB	10 dB
	Detection Pings, $5\log_{10} n$	3 dB	3 dB	3 dB	3 dB
	Poisson Scan Rate, λ	0.2 scan/s	0.5 scan/s	1.0 scan/s	25 scan/s
Calculated	Attenuation Coefficient, a	52 dB/km	104 dB/km	287 dB/km	287 dB/km
	Directivity Index, DI				
	Transmit	16 dB	24 dB	24 dB	27 dB
	Receive	39 dB	24 dB	24 dB	27 dB
	Source Level, SL	197 dB	207 dB	206 dB	204 dB
	Ambient or Self Noise, N	34 dB	41 dB	45 dB	44 dB
	Target Strength, TS	-30 dB	-30 dB	-30 dB	-30 dB
	Figure of Merit, FOM	**72 dB**	**66 dB**	**64 dB**	**49 dB**

has lesser impact at higher frequencies), we use conservative values of $N = 41$ dB and $N = 45$ dB, respectively.

Finally, we estimate the Poisson Scan rate for both sonar models by scaling the maximum update rate specified by the manufacturer. Assuming that these listed values apply to a sonar operating at its minimum optimal range, we scale the listed values by the nominal operating ranges used in our problem. For the P450-90 and P900-90 sonars, we estimate scan rates of $\lambda = 0.5$ and $\lambda = 1.0$ scans per second, respectively, based on nominal operating ranges of 200 and 100 m. These values agree with practical update rates observed when deploying these sensors on a REMUS AUV. The parameters used to model the P450-90 and P900-90 blazed array sonars are listed in Table VI alongside the parameters for the cylindrical FLS. The resulting FOM values calculated for these models are 66 and 64 dB, respectively.

F. SSS Model

Next, we estimate a FOM for a short-range side-looking sonar similar to the SSS used on the NPS REMUS 100 AUV. This type of sensor is representative of high-resolution sonars used to reacquire previously detected MLOs and identify them for subsequent neutralization [4]. Following the design example for a SSS in [68, Ch. 10], we use manufacturer specifications to derive a model for a 900-kHz SSS [71]. In contrast with the FLSs considered in Section III-E, this sonar transmits

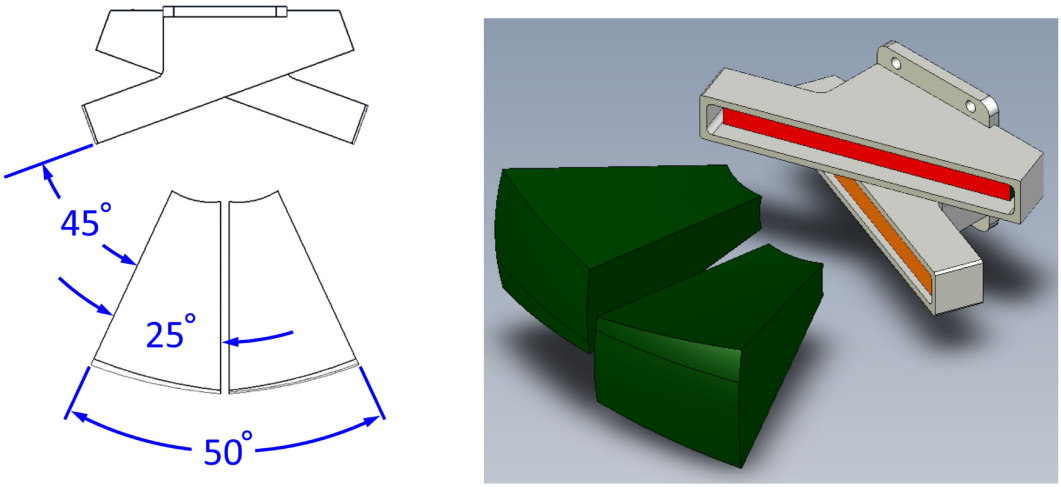

(a) (b)

Fig. 19. Blazed array FLS with 50° horizontal FOV constructed from two staves. (a) Top view. (b) 3-D beam pattern. Adapted from [90].

a CW pulse with duration $T = 6.67\,\mu$s and bandwidth $B = 1/T =$ 150 kHz. It also has a very narrow horizontal FOV and a wide vertical FOV. As before, the expression in [68, Table 2.3] is used to compute the number of elements in a line array from its beamwidth $n = 100/\text{BW} = 100/0.4 = 250$. Substituting n into (30), we calculate the directivity indices for the SSS's transmit/receive arrays: $\text{DI}_t = \text{DI}_r = 27$ dB.

Assuming that the sonar radiates 4 W of acoustical power, the SL for this sonar is SL = 204 dB, using (28). The attenuation coefficient and thermal agitation noise are computed from the 900 kHz operating frequency as $a = 287$ dB/km and $N_{\text{therm}} = N = 44$ dB, respectively, since underwater platforms have much lower self-noise than surface craft. Because the ping rate of SSS is usually determined by the vehicle platform's speed and the sonar's range setting [92], we estimate a Poisson Scan rate for this sonar based a sound speed of 1500 m/s and the two-way time required to travel the nominal operating range of 30 m: $\lambda = (1500\,\text{m/s})/(2 \times 30\,\text{m}) = 25$ scans per second. The parameters used to model this 900-kHz SSS are listed in Table VI and yield a FOM of 49 dB.

G. Model Verification and Validation

The sonar models developed in Sections III-E and III-F are simulated to verify that detection performance matches their SE, FOV geometry, and Poisson Scan rate characteristics. We assume no prior information, hence a mine might be found uniformly anywhere within the 2000 m $\times$ 2000 m search area shown in Fig. 20. The color map represents the probability of nondetection at each location, where the maximum P_{ND} value (dark red) is a function of search area size. Search effort reduces P_{ND}. For example, Fig. 21 illustrates the portion of the search area covered by a USV with nominal 200-kHz FLS following the trajectory shown. P_{ND} approaches zero (blue) in areas covered by the sonar, indicating a high probability of detecting mines in those areas. Note that the swath width produced by this sensor model is approximately equal to twice the nominal range, as expected. At the end of the mission ($T_f = 1000$ s), the probability of nondetection $P_{\text{ND}}(T_f)$, conditioned over the entire search area, measures the residual MCM risk.

Similarly, Fig. 22 depicts an example trajectory for an AUV with SSS. To accommodate the AUV's slower speed and shorter sonar range, this simulation utilized a much smaller 400 m $\times$ 400 m search area. As a result, maximum P_{ND} values are higher because the uniform probability is distributed over a smaller area. Nevertheless, the relative color scale

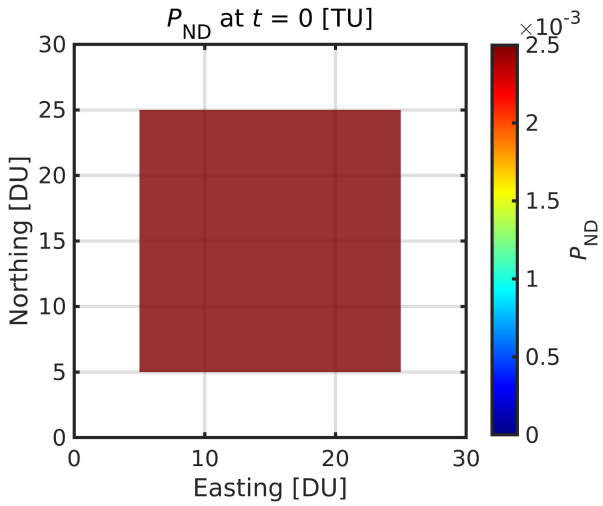

Fig. 20. Search area with uniform probability distribution, representing no prior target location data.

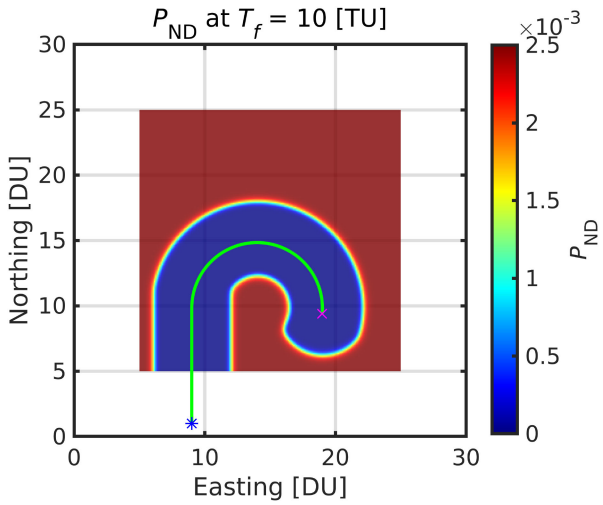

Fig. 21. Simulated search trajectory by a USV with 200-kHz FLS.

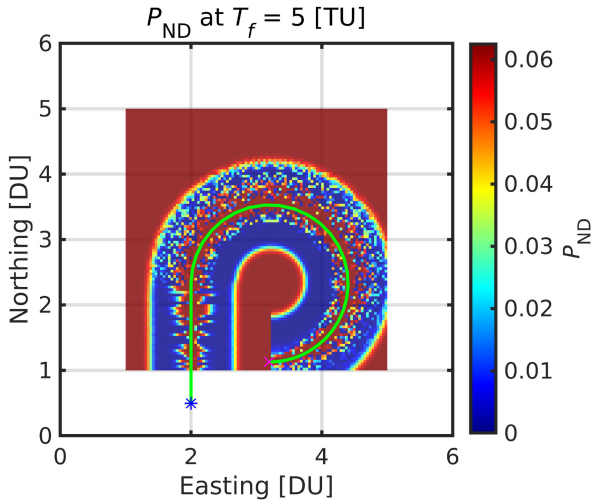

Fig. 22. Simulated search trajectory by an AUV with SSS.

indicates that our sidescan detection model is consistent with observed sidescan performance. Namely, the model provides little to no sonar coverage in the AUV's near-nadir region and detection performance is severely degraded during turns.

IV. Application: Time-Limited Optimal Search

Computational optimal search can be tailored to model and solve many different MCM problems of interest. Optimal solutions, obtained through simulation, provide performance benchmarks that can inform mission planning under real-world resource limitations. These resources include the number and type of autonomous vehicles at the MCM commander's disposal, as well as the sensors these platforms can carry. Typically, however, the most important resource is time. As Washburn and Kress note

> The great questions in search all involve time. We ask, "How long will detection take?" Or "What is the probability of detection in a fixed time?" Detection is inevitable, given sufficient time. The object of search planning is to speed things up [2, p. 134].

Indeed, while a number of planning algorithms have been developed to achieve complete coverage of a search area (see, e.g., [93] and [94]), most do not explicitly consider the ramifications of time. Instead, time is a byproduct of the search vehicle's velocity and spatial trajectory. A common metric is the area coverage rate, computed by multiplying a sensor's nominal sweep width by platform velocity. One example described in [95] derives a lower bound for the time required by an aerial vehicle to follow a flight plan that achieves complete sensor coverage. This type of bound can be informative when there is sufficient time to execute a given motion plan, but provides no guidance for adjusting the plan if the bound exceeds the allowable mission duration.

When time is limited and complete coverage is impossible, deterministic search patterns (e.g., lawnmower or box-spiral trajectories) are faced with two choices: execute the original motion plan as long as possible to achieve 100% sensor coverage in a subset of the entire search area; or adjust the track spacing to survey the entire search area, but with incomplete coverage. For a perfect "cookie cutter" sensor and uniform target pdf, both choices are equivalent and the probability of nondetection equals the fraction of unexplored area. Time-limited MCM operations can only reduce this risk by leveraging prior information about the target distribution. If it is known, for example, that mines have been deployed in an "evenly spaced mine line," Stack and Smith [96] proposed a track-spacing method that yields a probability of missed mines below the unexplored area ratio.

Mission time is a hard constraint in most MCM operations, motivating the fixed-time problem formulation described in Section II. We seek time-limited optimal search trajectories that minimize MCM risk for a given vehicle, sensor, and mission duration—whether or not prior information is available. In this section, we demonstrate the flexibility of the GenOC framework by solving MCM search problems for both cases. The optimal search problems explored in this article assume the following:

1) targets are bottom mines with known TS;
2) seafloor is flat;
3) water depth is constant;
4) search effort is confined to a rectangular area;
5) available mission time is fixed.

Sections IV-A and IV-B provide two examples of time-limited optimal search. First, we implement a wide area survey to detect and localize MLOs. Such missions are typically conducted during the initial phase of an MCM operation. Lacking prior information, we make the conservative assumption that targets have a uniform pdf and solve an optimal search problem. We then compare the time-limited search performance, i.e., MCM risk versus allotted mission time, for optimal trajectories against well-known deterministic search patterns. Second, we implement an RID mission and solve an optimal search problem for a vehicle to revisit a previously detected target location described by a joint normalized beta distribution. Finally, we compare optimal trajectories computed for different time and/or spatial discretizations. To make these comparisons, however, we recompute their objective values using a common baseline of 500 time nodes and a grid with 25×25 spatial nodes. We accomplish this by the following:

1) interpolating the solver's control input trajectory onto a fine grid of 500 time nodes;
2) propagating this finely gridded control input through the vehicle's EOM, using MATLAB's ode45 solver to generate finely gridded state trajectories;
3) recalculating the objective function for the dynamically feasible fine-grid state trajectories.

A. Search With No Prior Information—Mine Survey

In this section, we consider the common MCM problem of planning survey missions to detect MLOs in the absence of prior information about the target distribution. Typically, this involves a labor-intensive process to divide the search area into separate homogeneous regions, and tasking individual MCM assets to cover each region with a deterministic search pattern based on nominal area coverage rates. Various tactical decision aids (TDAs) have been developed to automate aspects of this process, and these information products can be "used by the force commanders to optimize the employment of naval assets in any particular tactical environment at sea" [66].

Many planning tools, e.g., Planning Aid for Tasking Heterogeneous Assets, can incorporate sonar performance models and time-based constraints to help mission planners determine the number of assets needed for a given mission [97]. However, these systems do not explicitly consider search vehicle dynamics and their attendant impact on detection performance. The GenOC framework takes this into account, providing a unique capability for planning MCM survey operations. The rest of this section applies the GenOC framework to plan a time-limited MCM survey for the following benchmark problem.

We wish to plan a 30-min MCM survey that has a 90% probability of detecting a bottom mine hidden anywhere in the 2000 m $\times$ 2000 m

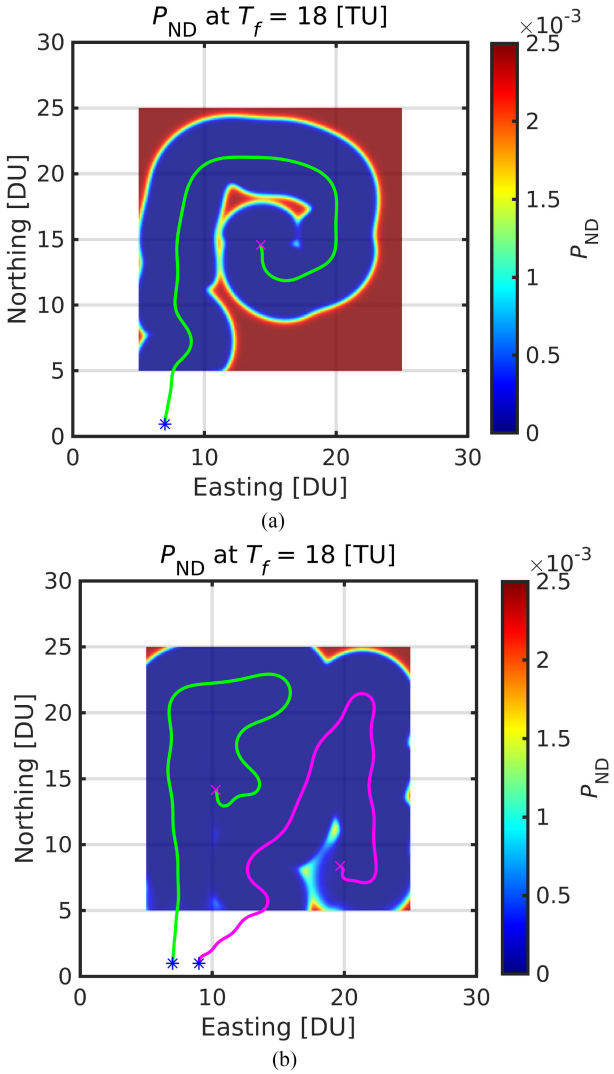

Fig. 23. Optimal trajectories for *SeaFox* USV(s) conducting a 30-min mine detection survey with 200-kHz FLS. (a) Single USV solution yields $P_{\text{ND}} = 0.362$ (computed with 30 time nodes). (b) Two USV solution yields $P_{\text{ND}} = 0.022$ (computed with 30 time nodes).

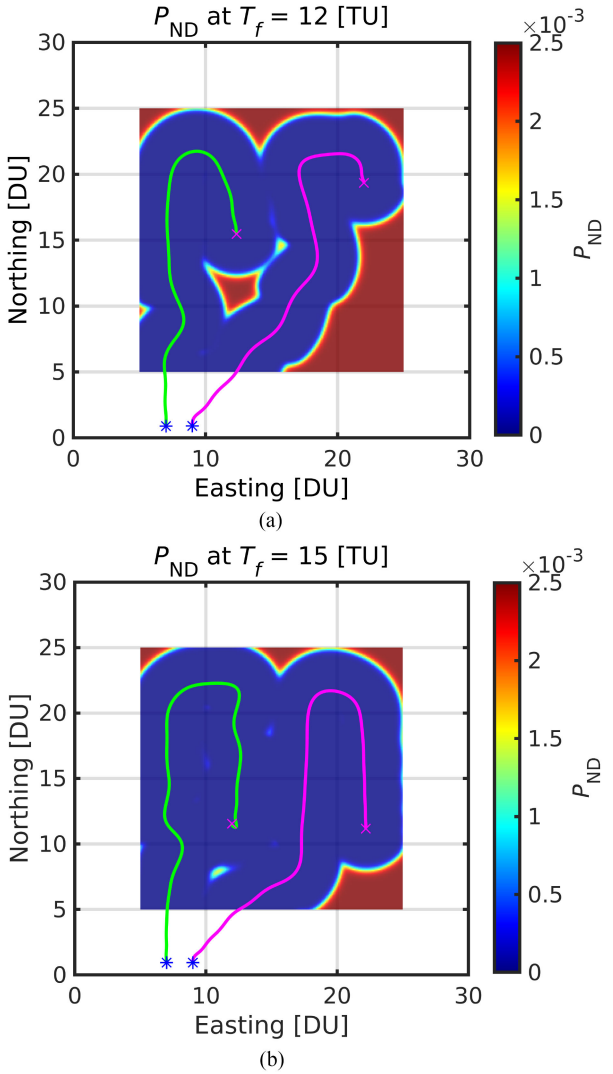

Fig. 24. Optimal trajectories for two *SeaFox* USVs conducting a 30-min mine detection survey with 200-kHz FLS. (a) 20-min mission yields $P_{\text{ND}} = 0.224$ (computed with 20 time nodes). (b) 25-min mission yields $P_{\text{ND}} = 0.087$ (computed with 30 time nodes).

search area shown in Fig. 20 with uniform probability distribution. We assume that the search area has a flat bottom and water depth is 20 m, and two *SeaFox* USVs equipped with 200-kHz FLS are available for this operation. After scaling this problem (see Section II-E) with DU = 100 m, TU = 100 s, and VU = 1 m/s, this objective corresponds to the risk threshold $P_{\text{ND}}(T_f = 18\,\text{TU}) \leq 0.1$. We first consider whether a single vehicle can meet this risk threshold, and solve an optimal search problem for a *SeaFox* USV launched from initial state vector $\vec{\mathbf{x}}(0) = [1\,\text{DU}, 7\,\text{DU}, 0\,\text{rad}, 0\,\text{rad/TU}]^\top$ and programmed to operate at constant velocity $V = 2.5$ m/s $= 2.5$ VU. A naive, yet feasible initial guess trajectory is provided to the solver using an open loop rudder step function to generate a right turn in the center of the search area. The optimal time-limited search trajectory is shown in Fig. 23(a), which achieves an objective value of $P_{\text{ND}}(T_f = 18\,\text{TU}) = 0.362$, computed on our $500 \times 25 \times 25$ discretization baseline. This trajectory resembles a box-spiral search pattern, although the limited mission duration does not permit full coverage. Nevertheless, this trajectory represents the best search performance that can be achieved by a single USV launched from the given initial condition. As such, it represents a local minimum, since different initial conditions may yield lower P_{ND} results. Monte Carlo simulation can be employed to determine the most favorable initial condition(s) for exploring a given search area. Due to the symmetry of this problem, however, such solutions are not unique. An initial condition of $\vec{\mathbf{x}}(0) = [23\,\text{DU}, 1\,\text{DU}, \pi/2\,\text{rad}, 0\,\text{rad/TU}]^\top$ will yield the same result.

Since the MCM survey failed to meet the desired risk threshold, the force commander must either increase the mission duration, or deploy additional search assets. Adding a second identical searcher launched from initial condition $\vec{\mathbf{x}}(0) = [1\,\text{DU}, 9\,\text{DU}, 0\,\text{rad}, 0\,\text{rad/TU}]^\top$ produces the optimal trajectories shown in Fig. 23(b), which reduce risk to $P_{\text{ND}}(T_f = 18\,\text{TU}) = 0.022$ in the same 30-min mission. This result suggests that two vehicles can meet the desired risk threshold of $P_{\text{ND}}(T_f = 18\,\text{TU}) = 0.1$ with a shorter mission duration. Additional simulations were conducted to determine whether two vehicles could achieve the survey objective in less time. Fig. 24(a) and (b) show the optimal trajectories computed for a 20-min and 25-min mission, respectively. The 20-min mission fails to meet our objective with time-limited $P_{\text{ND}}(T_f = 12\,\text{TU}) = 0.224$. The 25-min mission, however, achieves

TABLE VII
OPTIMAL TIME-LIMITED TRAJECTORIES FOR MINE DETECTION USING *SEAFOX* USVS WITH 200-kHz FLS

Number of USVs	Mission Duration	Time Nodes	P_{ND} $500 \times 25 \times 25$	Figure Reference
1	1800 s	30	0.362	Fig. 23 (a)
2	1200 s	20	0.224	Fig. 24 (a)
	1500 s	30	0.087	Fig. 24 (b)
	1800 s	30	0.022	Fig. 23 (b)

$P_{\text{ND}}(T_f = 15\,\text{TU}) = 0.087$, greater than 91% detection probability. Results from these simulations are summarized in Table VII.

B. Search With Prior Information—Mine Reacquisition

During the initial phase of an MCM operation, wide area surveys are conducted to detect MLOs in the environment that pose a threat to naval forces. These surveys can produce data sets with dozens of potential target locations, so it is critical to distinguish actual mines from harmless clutter before launching time-intensive neutralization missions. Successful target identification requires high-resolution sensors not typically carried on the initial survey vehicles, and these sensors are more effective at close range. As a result, follow-on missions are conducted to revisit the MLOs with AUVs carrying imaging sonars or video cameras. This type of RID mission incorporates prior information about MLO locations provided by the survey, but these data are uncertain; its accuracy depends upon the sensing and navigational performance of the survey vehicle itself. The vehicle should expect to search for the target upon arrival at the surveyed location. We therefore cast the motion planning problem for an RID mission as an optimal search for a target whose probability density is more informative than the uniform density assumed for the initial MCM search.

In this section, we apply the GenOC framework to solve RID problems. We assume that a prior survey has detected and localized an MLO with probability density described by a joint normalized beta distribution in two dimensions (see Section II-C). Using the same problem scaling and 20 DU $\times$ 20 DU search area, we select (α, β) parameter values of [8 DU, 16 DU] in the north direction and [16 DU, 8 DU] in the east direction. Substituting these values into (3) produces the 2-D pdf shown in Fig. 25, pictured before the RID mission begins. Our objective value, the residual risk of nondetection, is plotted on a color scale in which high probabilities are shown in dark red, and low probabilities are shown in blue. This β distribution corresponds to a previously detected target located at $[\omega_x,\ \omega_y] = [12\ \text{DU}, 19\ \text{DU}]$.

We wish to compute the time-limited optimal trajectory for a 40-min RID mission by a REMUS 100 AUV equipped with high-resolution imaging sonar. For this problem, we assume that the search area shown in Fig. 25 has a flat bottom and the AUV operates with constant velocity $V = 1.5$ m/s at altitude $h = 3$ m above the seafloor. The AUV is programmed to launch from a start location at $[x, y] = [1\ \text{DU}, 7\ \text{DU}]$ on an initial heading of 45°, utilizing prior information about the expected target location [12 DU, 19 DU]. From the AUV's initial state vector $\vec{\mathbf{x}}(0) = [1\,\text{DU}, 7\,\text{DU}, \pi/4\,\text{rad}, 0\,\text{rad/TU}]^\top$, we select a naive yet feasible initial guess trajectory that uses an open-loop rudder step function to generate a wide right turn.

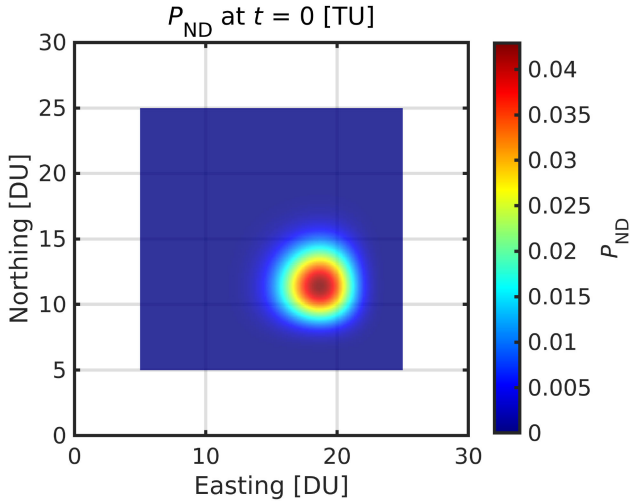

Fig. 25. Normalized beta distribution for a previously detected target located at [12 DU, 19 DU].

TABLE VIII
OPTIMAL TIME-LIMITED RID TRAJECTORIES FOR A REMUS 100 AUV WITH FLS AND $T_f = 2400$ S

Imaging Sonar	Time Nodes	P_{ND} $500 \times 25 \times 25$	Figure Reference
P450 FLS	20	0.012	Fig. 26 (a)
	35	0.001	Fig. 26 (b)
P900 FLS	30	0.333	Fig. 27 (a)
	40	0.305	Fig. 27 (b)

Simulated AUV search performance for the 450 and 900-kHz blazed array FLS models from Table VI are compared in Figs. 26 and 27, respectively. To compare solutions generated using a different number of time nodes, objective values have been recomputed using our $500 \times 25 \times 25$ discretization baseline. Results from these simulations are summarized in Table VIII.

The 20-time-node trajectory in Fig. 26(a) makes two parallel passes over the search area and then loiters over the expected target location for the remainder of the mission. The 35-time-node trajectory shown in Fig. 26(b) is more dynamic, approaching the search area from several different headings and almost encircling the expected target location. The 450-kHz blazed array FLS has a nominal operating range of 200 m, and an AUV using this sensor for RID missions can reduce the residual risk of nondetection to roughly 1% or less.

If a given mission requires a higher resolution sonar to achieve positive target identification, the same AUV can deploy a 900-kHz blazed array FLS instead. Example trajectories are provided in Fig. 27. The 30-time-node trajectory shown in Fig. 27(a) executes three symmetric loops over the expected target location, whereas the 40-time-node trajectory shown in Fig. 27(b) sweeps the target area with parallel tracks oriented on two distinct headings. Both solutions achieve a probability of nondetection around 30%, indicating that the 900-kHz sonar is hampered (in coverage) by its 100-m nominal range. Nevertheless, the GenOC framework produces trajectories that revisit the target area

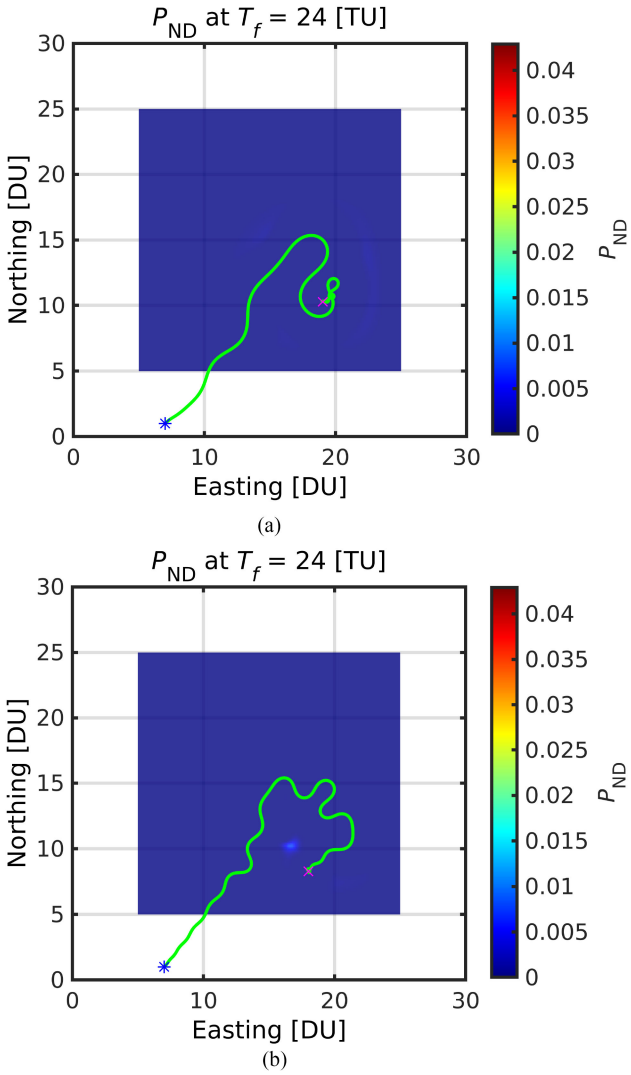

Fig. 26. Optimal RID trajectories for a REMUS AUV with P450 FLS. (a) $P_{ND} = 0.012$ (20 time nodes). (b) $P_{ND} = 0.001$ (35 time nodes).

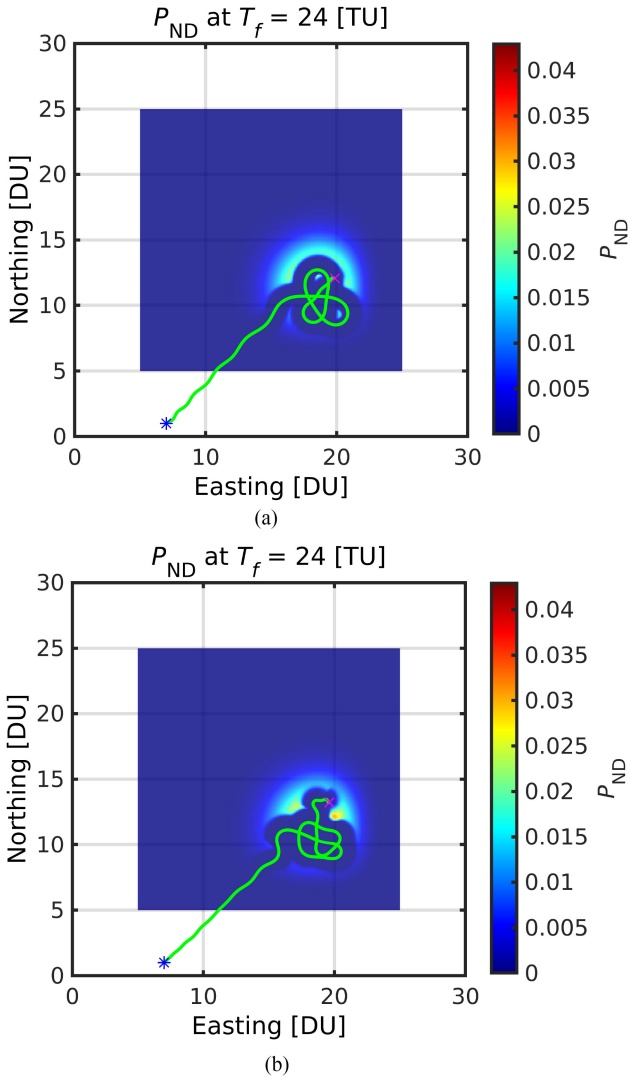

Fig. 27. Optimal RID trajectories for a REMUS AUV with P900 FLS. (a) $P_{ND} = 0.333$ (30 time nodes). (b) $P_{ND} = 0.305$ (40 time nodes).

repeatedly until the mission time expires. These solutions have similarities with traditional RID search patterns, which implement partial lawnmower swaths, aligned on different headings, to cover a target from multiple aspect angles for improved classification performance [11].

V. Analysis: Simulated Optimal Search Performance

A. Search Performance Versus Mission Duration

There is an inherent time dependence in the exponential detection model incorporated into the objective functions (8) and (11) in Section II. This model produces diminishing returns on search effort applied to previously visited regions of the operating area. Optimal search can leverage this property to produce motion plans which accomplish both *exploration*, when we wish to acquire information about the environment (see Section IV-A), and *exploitation* of all relevant prior information (see Section IV-B). We have already seen how mission duration impacts the optimal vehicle trajectories and achievable search performance for a given mission. While it is intuitively obvious that searching for longer periods of time can lower MCM risk, the ability to rapidly solve *optimal* search problems allows MCM commanders to quantitatively address questions such as the following.

1) What is the residual risk after searching for a fixed duration with a given vehicle and sensor combination?
2) How long will it take a search vehicle to reach a desired risk threshold with a given sensor payload?
3) How much time can be saved by employing multiple search assets?

Using the GenOC framework, we conduct several simulated experiments to solve a given optimal search problem for different values of our fixed mission duration. Subsequent Monte Carlo analysis can identify trends in the results to help characterize the optimal performance of a given system configuration as a function of time. Note that our current computational framework was written to solve GenOC problems with fixed final time; at present, we rely on Monte Carlo simulations to answer questions regarding the minimum time to reach a given risk threshold, for example. Future work will investigate the use of optimal control software packages, such as DIDO [98], which can address minimum-time problems directly, for solving this class of GenOC problems.

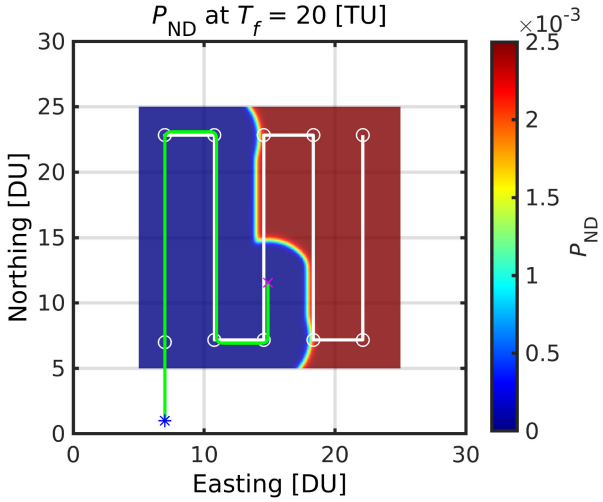

Fig. 28. Partially completed lawnmower survey pattern for $T_f = 2000$ s.

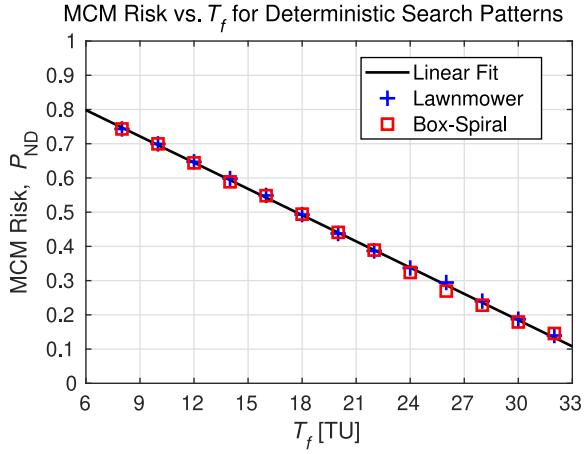

Fig. 29. Lawnmower and box-spiral pattern search performance versus mission duration.

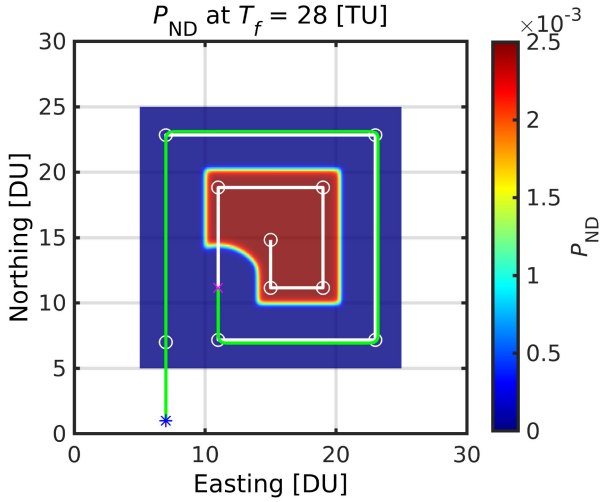

Fig. 30. Partially completed box-spiral survey pattern for $T_f = 2800$ s.

Two minor complications arising from this approach must be addressed. First, the numeric solution to any given optimal control problem is repeatable over multiple runs. To facilitate a meaningful statistical analysis, we must inject random variation into the simulations. Therefore, the position and heading angle of each search vehicle at $t = 0$ is randomized before each simulation, which influences the initial guess trajectories as well. Second, we must impose a feasibility check on the solver's output so that infeasible solutions are excluded from the analysis.

It is instructive to compare the search performance versus mission duration of our optimal search trajectories against well-known deterministic search patterns. For the single-USV survey mission described in Section IV-A, the following sections describe the feasible lawnmower and box-spiral trajectories which provide benchmarks for comparison.

1) Manually Specified Lawnmower Pattern: Computing the shortest path for a lawnmower coverage pattern to completely cover a polygonal area has been found to be NP-hard; as a result, approximate algorithms are proposed to plan efficient lawnmower trajectories in [99]. Additional examples are proposed in [100], which minimizes the number of turns along the path, and Huang [101] suggested that these patterns are time optimal for a robotic lawnmower.

We wish to generate a benchmark lawnmower trajectory that completely covers the 2000 m $\times$ 2000 m search area of Fig. 20 in the manner that an MCM operator programs a waypoint-based mission for a given sensor sweep width. The 200-kHz FLS used in our example has a nominal range of 400 m, so we select waypoints that place north/south-aligned track lines with 400-m track spacing, offset by 200 m from the search area's east/west boundaries. Whereas a SSS survey would perform the necessary U turns outside the search area, we assume that the FLS does not incur a performance penalty for turning motions [i.e., $F_r(\vec{\mathbf{x}}) = 1$]. Therefore, the long track lines are connected by short legs offset 200 m from the search area's north/south boundaries to avoid wasted effort. This waypoint pattern is denoted by white circles in Fig. 28.

Using our previous problem scaling, initial condition $\vec{\mathbf{x}}(0) = [1\text{ DU}, 7\text{ DU}, 0\text{ rad}, 0\text{ rad/TU}]^\top$ allows the USV to begin its mission prealigned with the first track line, thereby minimizing unnecessary path length. We ensure feasibility of this lawnmower pattern by constructing its 90° turns with clothoid curves (see Appendix C) and propagating a control input through the EOM, producing the green state trajectory in Fig. 28. This trajectory was used to recalculate P_{ND} on our 500 $\times$ 25 $\times$ 25 discretization baseline for different values of T_f, plotted as blue crosses in Fig. 29, where each data point represents an entire mission that completes as much of the lawnmower pattern as possible in the time available.

A linear fit of the P_{ND} and T_f data produces the formula

$$P_{\text{ND}}(T_f) = -0.000254(T_f) + 0.951. \tag{31}$$

Equation (31) confirms that $P_{\text{ND}}(T_f) \approx 1$ for $T_f = 0$ s, a trivial mission with no search effort; and $P_{\text{ND}}(T_f) = 0$ for $T_f \approx 3745$ s, sufficient time to completely cover the search area.

2) Manually Specified Box-Spiral Pattern: Spirals are another popular deterministic search pattern, and box spirals are very similar to the lawnmower trajectories discussed previously. While both patterns achieve complete coverage, Hsu and Lin [101] suggested box spirals as a minimal-energy alternative to time-optimal lawnmower patterns, since box spirals require less turning effort. Using the same assumptions, waypoint spacing, and initial condition as in Section V-A1, we generate a benchmark box-spiral trajectory that completely covers the 2000 m $\times$ 2000 m search area of Fig. 20. The feasible state trajectory for this pattern is shown as a green line in Fig. 30, whereas the waypoint pattern is denoted by white circles.

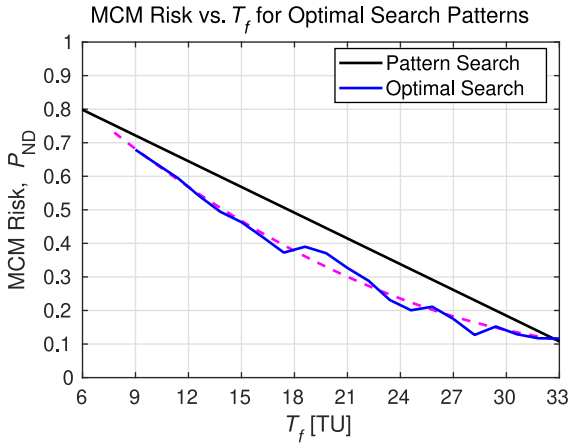

Fig. 31. Performance comparison between optimal search trajectories and exhaustive search patterns.

Box-spiral $P_{\text{ND}}(T_f)$ values, recalculated on our $500 \times 25 \times 25$ discretization baseline, are plotted as red squares in Fig. 29 for different values of T_f. As before, each data point represents an entire mission that completes as much of the box-spiral pattern as possible in the time allotted. This data reveal a linear relationship nearly identical to the lawnmower pattern, and the best linear fit yields the formula

$$P_{\text{ND}}(T_f) = -0.000257(T_f) + 0.952. \tag{32}$$

The mean of the lawnmower and box-spiral patterns' linear fits are depicted by a black line with constant slope in Fig. 29. A constant slope is expected, since lawnmower and box-spiral trajectories implement "exhaustive search." Recall that exhaustive search with a definite range sensor yields a detection probability P_{D} equal to the coverage ratio, the fraction of search area covered by the sensor. Therefore, a "cookie cutter" sensor with sweep width W, mounted on a vehicle moving at constant velocity V, in a search area A, produces a probability of detection $P_{\text{D}}(t) = W\,V\,t/A$ that is linear with time [21, Ch. 2, p. 4]. We have simply plotted the complement, $P_{\text{ND}}(T_f) = 1 - P_{\text{D}}(T_f)$, in Fig. 29.

3) Optimal Search Trajectories From Solver: Monte Carlo simulations were conducted for the mine survey problem of Section IV-A to analyze the optimal search performance for a range of mission durations between 15 and 60 min, spaced at 2-min intervals. Using our previous problem scaling, ten simulations were conducted for each value of T_f, with initial states drawn from a uniform $\mathcal{U}$(min., max.) or normal $\mathcal{N}$(mean, std. dev.) probability distribution as follows:

$$\begin{aligned} x(0) &\sim \mathcal{U}(0, 0.1) \text{ DU} \\ y(0) &\sim \mathcal{U}(0.5, 2.5) \text{ DU} \\ \psi(0) &\sim \mathcal{N}(0, \pi/12). \end{aligned} \tag{33}$$

Initial turn rate $r(0) = 0$. The initial guess is computed from an open-loop rudder step input that commands a right turn when $y(0)$ is in the western half of the search area, and commands a left turn when $y(0)$ is in the eastern half of the search area.

The mean objective values of P_{ND} from the ten simulations conducted for each value of T_f are plotted as the blue line in Fig. 31, while a quadratic curve fit to these data is shown as the dashed magenta line. The mean of the two deterministic search patterns derived previously is shown as a black line for comparison purposes. The plots intersect at roughly $T_f = 3280$ s and an objective value of $P_{\text{ND}} = 10\%$. This plot clearly indicates that an optimal search strategy outperforms deterministic exhaustive search patterns for time-limited missions less than about 55 min in duration. However, it also suggests that operators would be better off selecting a deterministic search pattern if there is sufficient time to execute it to completion.

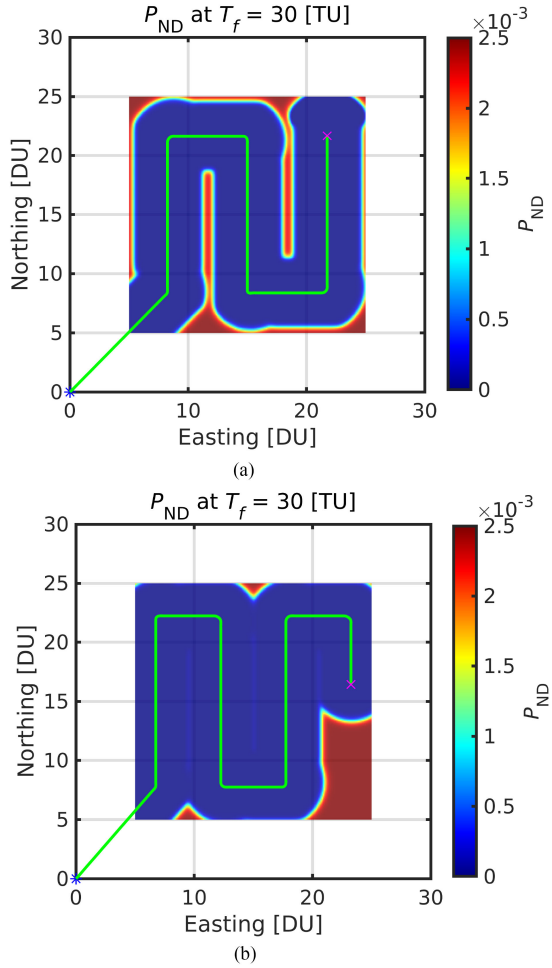

Fig. 32. Lawnmower search results for a single USV with FLS when mission time is limited to $T_f = 3000$ s: (a) 675-m track spacing leaves coverage gaps; (b) 550-m track spacing achieves near-optimal time-limited search performance.

B. Optimal Lawnmower Pattern Lane Spacing

Numerous simulations (see Fig. 31) have verified that GenOC trajectories outperform exhaustive search patterns with constant track spacing, particularly under time or resource constraints. However, most unmanned vehicle missions are still specified by a set of waypoints that denote a lawnmower search pattern, since straight and level motion along parallel track lines produces the best sidescan or SAS imagery. In such cases, optimal trajectories can be used to establish performance benchmarks for conventional mission planning methods.

Specifically, for a given sonar and mission duration, it is usually possible to select a constant lawnmower track spacing that approaches the optimal search performance benchmark computed by GenOC. For example, Fig. 32(a) and (b) illustrate 50-min (time-limited) search performance for lawnmower patterns with track spacing of 675 and 550 m, respectively. The 675-m track spacing is suboptimal for the given scenario, leaving gaps in sonar coverage, while the 550-m track spacing does not. In this manner, near-optimal lawnmower search performance

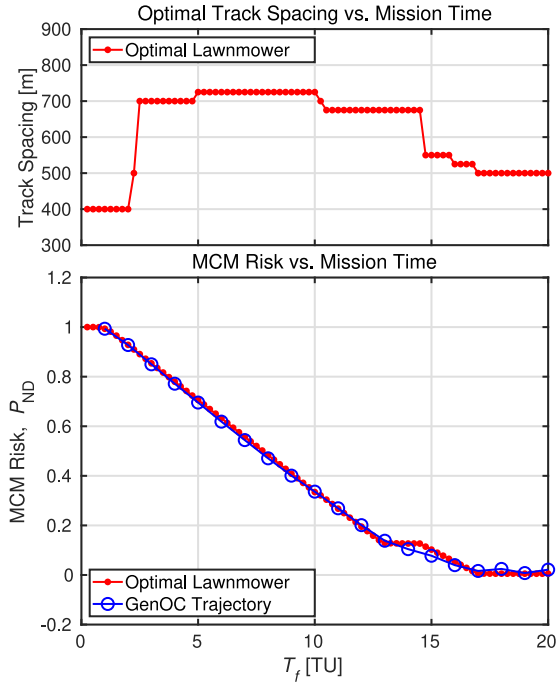

Fig. 33. Performance comparison between optimal search trajectories and lawnmower patterns with near-optimal track spacing.

for a range of track spacing values can be plotted as a function of mission duration in Fig. 33. The upper plot indicates track spacing values corresponding to the best lawnmower search performance in the lower plot (red), as compared with the optimal GenOC trajectory (blue). This type of analysis can also be used as a mission planning tool to recommend the best lawnmower track spacing for a given vehicle, sensor, and mission profile.

C. Search Performance Versus Time Discretization

One of the most important aspects of motion planning in a computational optimal control framework is the choice of discretization scheme, as this directly impacts accuracy and computational run time. In general, numeric trajectory approximations converge to their continuous counterparts as the number of computational nodes increase [102], [103]. While increasing the number of nodes can improve solution accuracy, designers must balance this accuracy against the computational demands required by high-node discretizations. Moreover, high-node control trajectory solutions may be infeasible for implementation on an actual vehicle system. A detailed theoretical discussion on this topic is beyond the scope of this article, but an excellent overview on pseudospectral optimal control theory is provided in [104], with convergence and consistency proofs given in [105].

Hurni recommended using "the lowest possible number of nodes for feasible and safe trajectories," and proposed a novel criteria for selecting the number of nodes based on the distance a ground vehicle must travel; and the size of the obstacles it must avoid along the way [58]. We have assumed an obstacle-free environment for MCM search planning. Moreover, we do not require real-time algorithms for dynamic replanning. Instead, we generate an optimal search strategy for the entire MCM mission, subject to any prior information we possess. The lack of a real-time constraint grants us the luxury of computing multiple solutions with increasingly fine discretization schemes in our search for an optimal and *feasible* search trajectory. Solutions whose feasibility cannot be verified by control trajectory propagation are rejected.

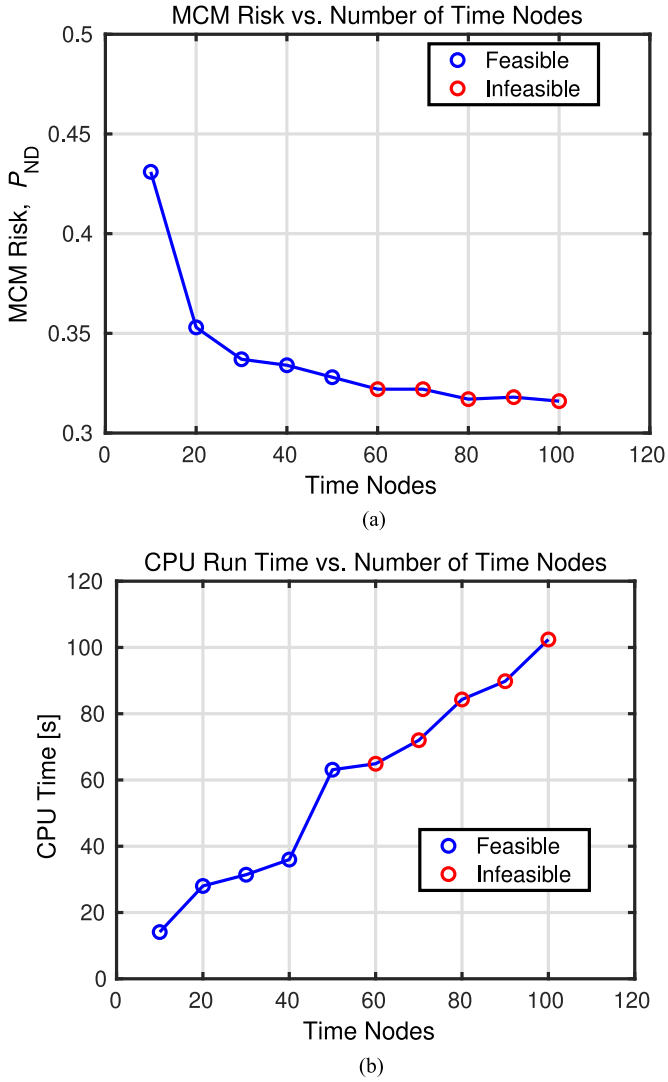

Fig. 34. Solver performance versus number of time nodes for a single-vehicle 30-min survey. (a) Solver-provided objective values. (b) CPU runtimes.

We will demonstrate this concept for the 30-min mine detection survey mission described in Section IV-A. Fig. 34(a) plots the objective values for ten optimal single-vehicle solutions, each computed at a different time discretization using n_t time nodes. We observe that as the number of time nodes increases, the numeric solution's objective value converges to $P_{\text{ND}} \approx 0.320$. The plotted objective values are the raw solver outputs, calculated directly from the n_t solution nodes, which we denote as J_{out}. Fig. 34(b) plots the times required to compute each solution using a 2.30-GHz Xeon CPU (complete processor specifications are listed in [106]). We note that there is a large increase in run time required to compute solutions with more than 40 time nodes, and the 50-node solution takes nearly twice as long as the 30-node solution. Moreover, the 40-node solution takes nearly 5 s longer to compute than the 30-node solution, yet only decreases P_{ND} by 0.003. For this reason, 30-node solutions were selected as an acceptable compromise for the plots presented in Section IV-A.

To support performance comparisons between different numeric solutions, solution trajectories must first be transferred onto a common discretization scheme. This is achieved by interpolating control trajectories, propagating state variables through the system's ODEs, and recalculating objective values on our $500 \times 25 \times 25$ discretization

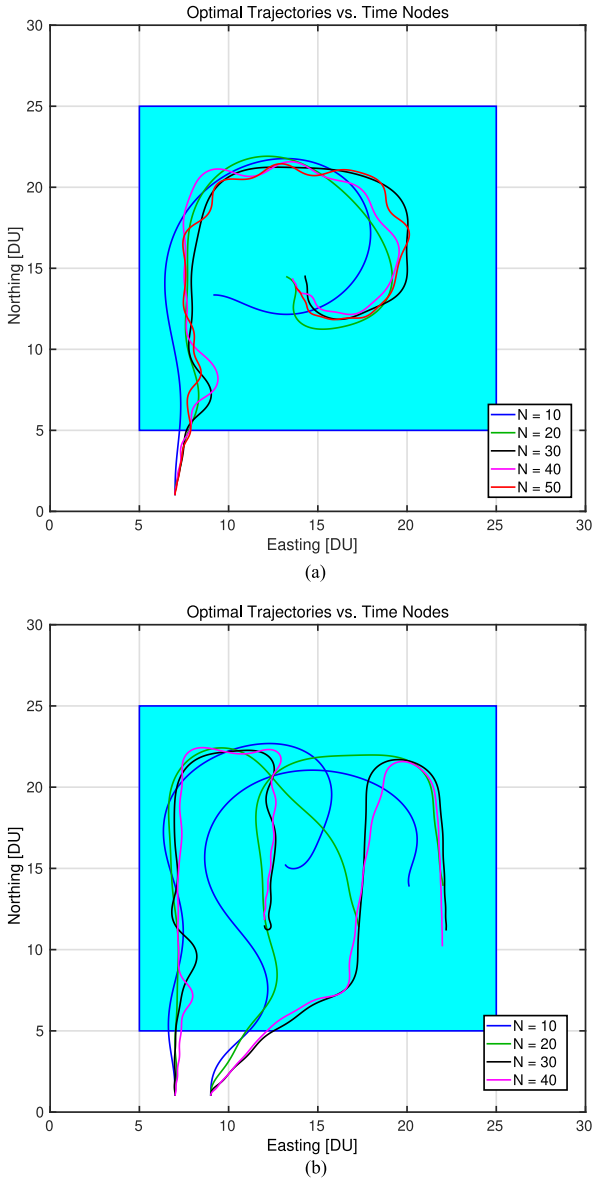

Fig. 35. Optimal search trajectories versus number of time nodes: (a) 30-min single-vehicle survey; (b) 25-min two-vehicle survey.

baseline. Objective values corresponding to these ODE-propagated state trajectories are designated by J_{ode}. Finally, the propagated trajectories are compared against the solution nodes to assess each solution's feasibility. In this example, all of the numeric solutions with greater than 50 nodes fail the feasibility criteria proposed in [58] and are therefore deemed infeasible. Feasible search trajectories from these single-vehicle simulations are illustrated in Fig. 35(a). By way of comparison, Fig. 35(b) shows feasible optimal trajectories computed with different numbers of time nodes for a 25-min two-vehicle mine detection survey.

Note that high-node solutions incorporate periodic turning motions into their trajectories. This has the benefit of aiming the vehicle's FLS to cover a larger portion of the search area, reducing the accumulated probability of nondetection. Recall that we have not penalized the detection rate of this FLS for turning motion as we would for an SSS, i.e., the shaping function $F_r(\vec{\mathbf{x}}) = 1$ for this problem. This increased complexity yields diminishing returns, however; the optimal trajectories computed using 30 or more time nodes are remarkably similar, and all of them achieve P_{ND} within 3% of the 50-node best performer. Table IX summarizes the search performance for all of these one- and two-vehicle survey trajectories.

VI. Conclusion

The key contribution of this article is the development of engineering-based sensor models for various sonars typically used in MCM. These models compute mine detection rate as a function of sonar design parameters and search vehicle trajectories. Next, the probability that searchers following these trajectories will fail to detect mines in an area of interest is used to quantify the residual risk after different MCM missions. We cast this risk as a GenOC objective function to be minimized over all feasible search trajectories that satisfy constraints imposed by vehicle dynamics. Examples are provided that illustrate this trajectory optimization approach, and initial results suggest that the GenOC solution framework is suitable for optimal motion planning of autonomous minehunting missions under temporal, spatial, and dynamic constraints. The authors are actively developing a mission planning tool for MCM based on this computational framework, and are working to expand the class of problems that can be solved using this approach.

Appendix

A. Nomoto Steering Model for REMUS 100 AUV

We derive a Nomoto steering model for the REMUS 100 AUV from the lateral steering equation in [46, eq. (118)]

$$\begin{bmatrix} m - Y_{\dot{v}} & -Y_{\dot{r}} & 0 \\ -N_{\dot{v}} & I_{zz} - N_{\dot{r}} & 0 \\ 0 & 0 & 1 \end{bmatrix} \begin{bmatrix} \dot{v}(t) \\ \dot{r}(t) \\ \dot{\psi}(t) \end{bmatrix} + \begin{bmatrix} -Y_v & mu_0 - Y_r & 0 \\ -N_v & -N_r & 0 \\ 0 & -1 & 0 \end{bmatrix} \begin{bmatrix} v(t) \\ r(t) \\ \psi(t) \end{bmatrix} = \begin{bmatrix} Y_{\delta_r} \\ N_{\delta_r} \\ 0 \end{bmatrix} \delta_r(t) \tag{A.1}$$

where

- $v(t)$ sway velocity in the y-axis direction;
- $r(t)$ yaw rate;
- $\psi(t)$ yaw angle;
- $\delta_r(t)$ rudder angle;
- m vehicle's mass;
- I_{ZZ} vehicle's moment of inertia about the z-axis;
- Y hydro. coefficients producing sway forces;
- N hydro. coefficients producing yaw moments.

In general, control inputs and state variables (and their derivatives) produce nonlinear hydrodynamic forces and moments. It is common practice, however, to approximate these effects by multiplying each contributing variable with a linearized hydrodynamic coefficient. In (A.1), Y and N denote coefficients that produce sway forces and yaw moments, respectively, while subscripts denote their corresponding control input or state variable. Assuming that sway velocity is zero

TABLE IX
OPTIMAL TIME-LIMITED SEARCH PERFORMANCE VERSUS THE NUMBER OF DISCRETE TIME NODES FOR MINE DETECTION SURVEY MISSIONS

No. of USVs	Mission Duration	Time Nodes	$J_{out} = P_{\text{ND}}$ $N \times 25 \times 25$	$J_{ode} = P_{\text{ND}}$ $500 \times 25 \times 25$	CPU Run Time	Trajectory Plot
1	1800 s	10	0.676	0.431	14.1 s	Fig. 35 (a)
		20	0.443	0.353	28.0 s	
		30	0.358	0.337	31.4 s	
		40	0.342	0.334	36.0 s	
		50	0.328	0.328	63.1 s	
2	1500 s	10	0.428	0.251	47.1 s	Fig. 35 (b)
		20	0.160	0.133	77.5 s	
		30	0.076	0.067	124.5 s	
		40	0.058	0.056	141.5 s	

(no sideslip), we rearrange (A.1) as

$$\begin{bmatrix} I_{zz} - N_{\dot r} & 0 \\ 0 & 1 \end{bmatrix} \begin{bmatrix} \dot r(t) \\ \dot\psi(t) \end{bmatrix} + \begin{bmatrix} -N_r & 0 \\ -1 & 0 \end{bmatrix} \begin{bmatrix} r(t) \\ \psi(t) \end{bmatrix} = \begin{bmatrix} N_{\delta_r} \\ 0 \end{bmatrix} \delta_r(t). \tag{A.2}$$

Manipulating the $\dot r(t)$ expression from (A.2) into the form of our first-order Nomoto steering model [see (1)], we have

$$\begin{aligned} (I_{zz} - N_{\dot r})\,\dot r(t) &= N_r\, r(t) + N_{\delta_r}\,\delta_r(t) \\ \dot r(t) &= \frac{N_r}{(I_{zz} - N_{\dot r})}\, r(t) + \frac{N_{\delta_r}}{(I_{zz} - N_{\dot r})}\,\delta_r(t) \\ \dot r(t) &= \frac{1}{T}\left[K\, u(t) - r(t)\right] \end{aligned} \tag{A.3}$$

where $T = (N_{\dot r} - I_{zz})/N_r$, $K = -N_{\delta_r}/N_r$, and $u(t) = \delta_r(t)$. Substituting values from [46] for the yaw axis moment of inertia I_{zz} and the hydrodynamic coefficients $N_{\dot r}$, N_r, and N_{δ_r} produces the REMUS 100 model parameters listed in Table II.

B. Problem Scaling

For our search problems, the vehicle models from Section II-A can be scaled by canonical units of distance (DU), time (TU), and velocity (VU = DU/TU) to produce dimensionless variables designated by overbar notation: $\overline{x} = x/\text{DU}$, $\overline{y} = y/\text{DU}$, $\overline{\psi} = \psi$, $\overline{r} = r/(1/\text{TU}) = (\text{TU})r$, $\overline{t} = t/\text{TU}$, and $\overline{u} = u$. Note that angular variables for heading ψ and control input $u = \delta_r$ (rudder angle) are already expressed in dimensionless units of radians. The chosen scaling must also be applied to constant model parameters, such as forward velocity V, as well as the gain K and time T constants of the Nomoto steering model: $\overline{V} = V/\text{VU}$, $\overline{K} = K/(1/\text{TU}) = (\text{TU})K$, and $\overline{T} = T/\text{TU}$. Substituting these expressions into our original expressions for x and y yields their state-space equations in nondimensional units

$$\begin{aligned} \dot x &= \frac{dx}{dt} = \frac{d(\text{DU}\,\overline{x})}{d(\text{TU}\,\overline{t})} = \frac{\text{DU}}{\text{TU}}\frac{d\overline{x}}{d\overline{t}} = \text{VU}\,\dot{\overline{x}} \\ \dot{\overline{x}} &= \frac{1}{\text{VU}}\dot x = \frac{1}{\text{VU}} V\cos\psi = \overline{V}\cos\overline{\psi}. \end{aligned} \tag{A.4}$$

Similarly, we have

$$\dot{\overline{y}} = \overline{V}\sin\overline{\psi}. \tag{A.5}$$

Likewise, scaling by canonical units for ψ and r yields the nondimensional expressions

$$\begin{aligned} \dot\psi &= \frac{d\psi}{dt} = \frac{d\overline{\psi}}{d(\text{TU}\,\overline{t})} = \frac{1}{\text{TU}}\frac{d\overline{\psi}}{d\overline{t}} = \frac{1}{\text{TU}}\,\dot{\overline{\psi}} \\ \dot{\overline{\psi}} &= \text{TU}\,\dot\psi = (\text{TU})\,r = \overline{r}, \text{ and} \\ \dot r &= \frac{dr}{dt} = \frac{d(1/\text{TU})\,\overline{r}}{d(\text{TU}\,\overline{t})} = \frac{1}{\text{TU}^2}\frac{d\overline{r}}{d\overline{t}} = \frac{1}{\text{TU}^2}\,\dot{\overline{r}} \end{aligned} \tag{A.6}$$

$$\begin{aligned} \dot{\overline{r}} &= (\text{TU}^2)\,\dot r = (\text{TU}^2)\frac{1}{T}\,(Ku - r) \\ &= (\text{TU}^2)\frac{1}{\text{TU}\,\overline{T}}\left(\frac{\overline{K}}{\text{TU}}\,\overline{u} - \frac{\overline{r}}{\text{TU}}\right) \\ &= \frac{1}{\overline{T}}\left(\overline{K}\,\overline{u} - \overline{r}\right). \end{aligned} \tag{A.7}$$

Equations (A.4) through (A.7) confirm that our scaling has not changed the underlying dynamics of the problem. To ensure the objective function J is calculated properly, physical units in the detection rate equation must also be scaled by the appropriate canonical units. The Poisson Scan rate λ is scaled using TU to yield the nondimensional form

$$\overline{\lambda} = \lambda/(1/\text{TU}) = (\text{TU})\lambda. \tag{A.8}$$

Recall from (17) that our range-dependent PL includes a spherical spreading term $20\log_{10}(\|\vec{\boldsymbol{\omega}} - \vec{\mathbf{x}}(t)\|)$ and an acoustical absorption term $a\|\vec{\boldsymbol{\omega}} - \vec{\mathbf{x}}(t)\|$. At each time t, we compute the distance D between a vehicle and target. Scaling this distance yields

$$\begin{aligned} D &= \|\vec{\boldsymbol{\omega}} - \vec{\mathbf{x}}\| \\ D &= \sqrt{(\omega_x - x)^2 + (\omega_y - y)^2 + (\omega_z - z)^2} \\ D &= \sqrt{(dx)^2 + (dy)^2 + (dz)^2} \\ D &= \sqrt{(\text{DU}\,\overline{dx})^2 + (\text{DU}\,\overline{dy})^2 + (\text{DU}\,\overline{dz})^2} \\ D &= \text{DU}\sqrt{\overline{dx}^2 + \overline{dy}^2 + \overline{dz}^2} \\ D &= \text{DU}\,\overline{D}. \end{aligned} \tag{A.9}$$

So $\overline{D} = D/\text{DU}$, as expected. The attenuation coefficient a has units of dB/m and must be scaled by canonical distance DU (dB represents a

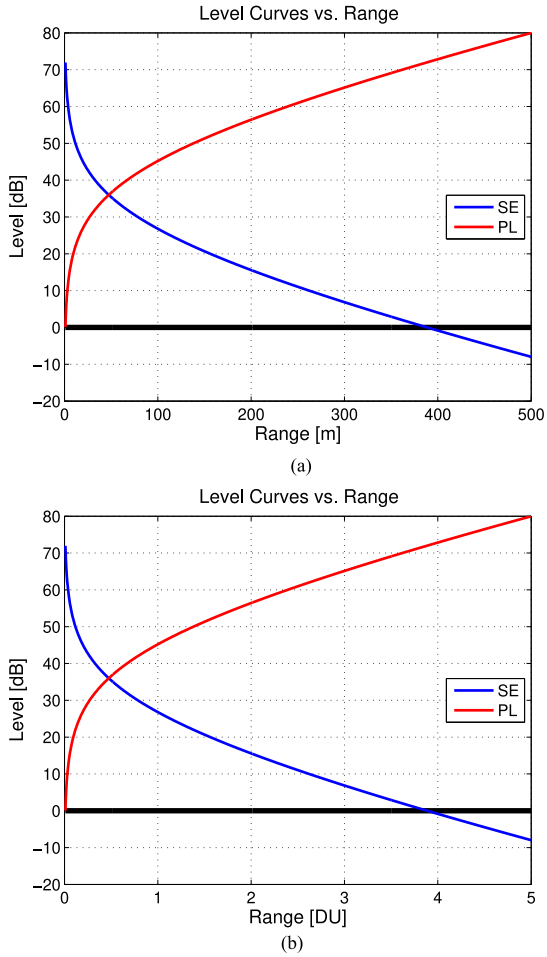

Fig. 36. PL and SE for a nominal 200-kHz FLS with FOM = 72 dB. (a) Physical range. (b) Nondimensional range.

ratio and is dimensionless already) as

$$\overline{a} = \frac{a}{1/\mathrm{DU}} = (\mathrm{DU})a. \tag{A.10}$$

Finally, the equation for PL in dB using dimensionless quantities becomes

$$\mathrm{PL}(D) = 20\log_{10}(D) + a(D) \tag{A.11}$$

$$\mathrm{PL}\left(\overline{D}\right) = 20\log_{10}\left(\mathrm{DU}\,\overline{D}\right) + \frac{\overline{a}}{\mathrm{DU}}\left(\mathrm{DU}\,\overline{D}\right)$$

$$\mathrm{PL}\left(\overline{D}\right) = 20\log_{10}\left(\mathrm{DU}\right) + 20\log_{10}\left(\overline{D}\right) + \overline{a}\left(\overline{D}\right) \tag{A.12}$$

which has an additional term due to the distance scale factor. The level curves in Fig. 36 verify that PL computed with (A.11) as a function of physical distance D [see Fig. 36(a)] is equivalent to PL calculated with (A.12) as a function of nondimensional distance $\overline{D}$ with DU = 100 m [see Fig. 36(b)]. These curves also show the SE versus range for the 200-kHz FLS with FOM = 72 dB, derived in Section III-E1. Note that SE is zero at a range of 400 m.

C. Initial Guess

When choosing an initial guess trajectory for numeric optimization, the guess should itself be a valid candidate solution to the problem of interest. This implies that the initial guess should

1) have the same initial condition $\vec{\mathbf{x}}(0) = \vec{\mathbf{x}}_0$ as the problem of interest;
2) have the same time node discretization as the problem of interest;
3) be feasible, i.e., obey state variable constraints and control limits.

The first two requirements are easy to address while encoding a problem of interest into the GenOC framework. Satisfying the feasibility requirement depends on the sophistication of the initial guess trajectory, which corresponds to the amount of prior information we wish to incorporate. Ideally, we would like to find an optimal solution without knowing beforehand what a "good" initial guess looks like. A trivial guess which satisfies the first two requirements, for example, would be a zero velocity trajectory that remains at $\vec{\mathbf{x}}_0$ for all time. Unfortunately, the constant velocity vehicle models defined in Section II-A do not permit acceleration, and the solver would be unable to find another solution trajectory. Similarly, a guess that specifies a trivial control trajectory $u(t) = 0$ for all time is infeasible under our definition, because the vehicle would travel at constant velocity and heading until it departed its operating area.

A naive open-loop control trajectory is a good compromise between a trivial (no information provided) guess, and an expert (full information provided) guess. For example, a rudder angle step function, executed at the proper time, will cause a search vehicle to turn in a circle until the end of the simulation. This has the benefit of keeping the vehicle in the search area and ensures that state variable limits are not exceeded. In practice, we approximate a discrete step function with a smooth sigmoidal curve centered at the step time [82]. This simple control trajectory is then propagated through the motion model, using a Runge–Kutta algorithm (e.g., the MATLAB ode45 solver) to calculate the corresponding state variable trajectories to ensure initial guess feasibility [see Fig. 37(a)].

If there is sufficient time to exhaustively search an area, an expert initial guess can be provided that completely covers the area with a deterministic search pattern. A number of algorithms for "coverage path planning" exist [93], based on sensor sweep width. Deterministic search patterns include spirals for searching circular areas [107]; and box spiral, lawnmower, or zamboni patterns for searching rectangular areas [108]. While these strategies may waste effort when the search area contains subregions with near-zero target probability distribution [109], it is usually possible to decompose the search area into smaller regions and avoid this situation. Moreover, for rectangular search areas, line sweeps conducted parallel to boundary edges are optimal for minimizing the number of turns required [100]. This fact, plus the ease of implementing these patterns with vehicle autopilots, explain the widespread use of lawnmower patterns for underwater search operations.

These rectangular coverage patterns require path following controllers to execute them. Coverage path planners often take this for granted, assuming that the search area can be decomposed into smaller, "easy to cover" cells; the vehicle need only visit all such cells to achieve complete coverage [93]. Another approach is to extend the line sweep track length by a vehicle-specific distance, assuming all 180° turns occur outside the search area and the vehicle reestablishes straight-line motion before reentry on an adjacent track [110]. While these approaches determine the geometric length, spacing, and number of track lines for a given sweep width, they do not represent feasible trajectories, per se.

To specify this type of coverage pattern as an initial guess trajectory for an optimal control problem, we must convert a waypoint-based specification into a feasible trajectory. Haugen suggested an approach for constructing a feasible lawnmower path which used clothoids as transition curves between waypoint segments. The clothoids are scaled such that a vehicle following this trajectory obeys feasibility constraints on its angular velocity and acceleration [111]. Depending on the track

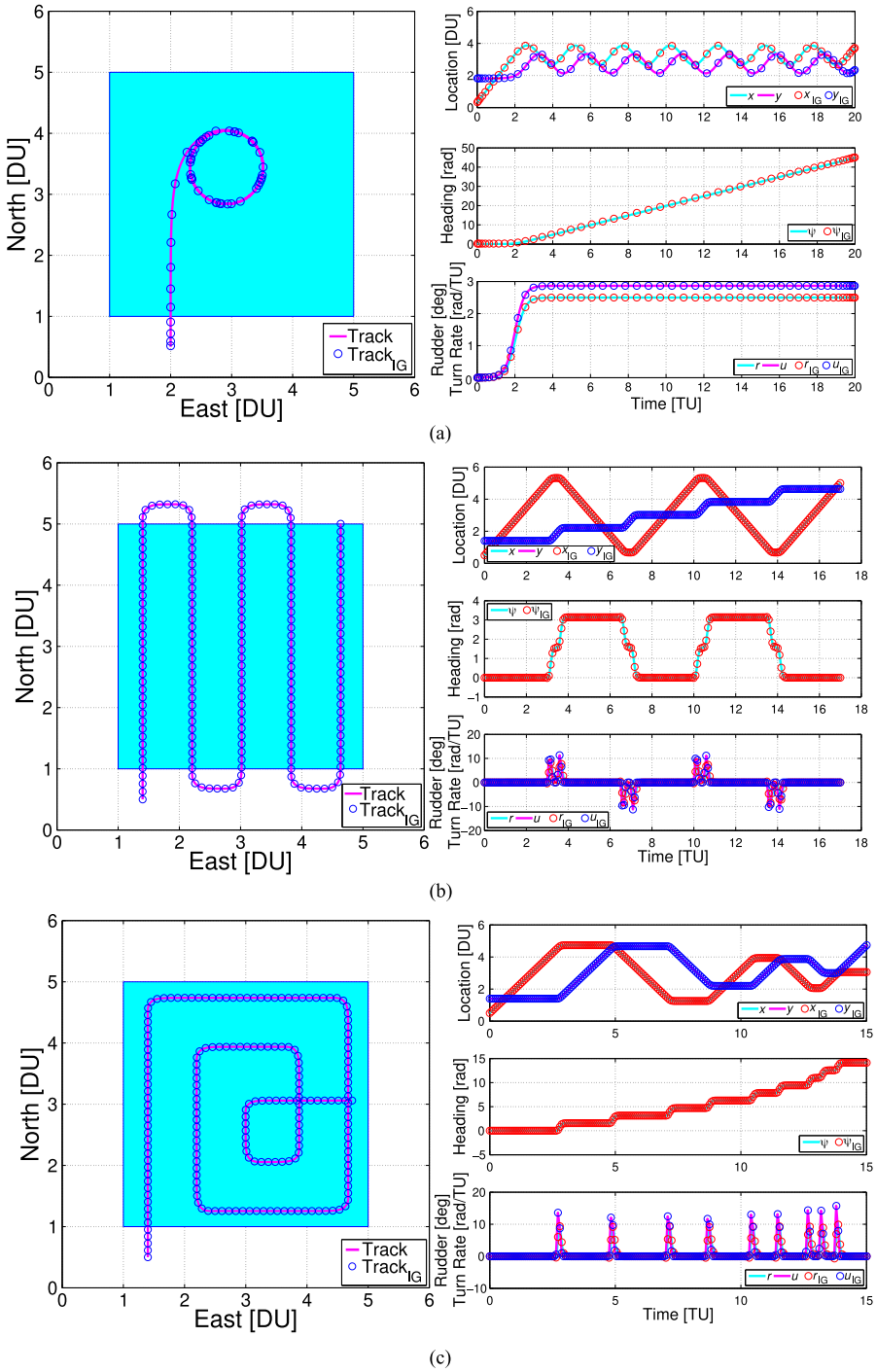

Fig. 37. Initial guess state and control trajectories. (a) Open-loop rudder step. (b) Lawnmower search pattern. (c) Box-spiral search pattern.

spacing and vehicle turning radius, one of three different U turn paths are constructed to connect adjacent line sweep tracks. For our search problems, we assume that the lawnmower track spacing permits a piecewise U turn comprised of two 90° clothoids and a straight line segment (Case A) [111]. This produces a feasible path in the horizontal plane, which can be converted into a control trajectory $u(k)$ by inverting the searcher model of Section II-A as follows:

$$\Delta x(k) = x(k+1) - x(k)$$
$$\Delta y(k) = y(k+1) - y(k)$$
$$\psi(k) = \text{atan2}\left(\Delta y(k),\ \Delta x(k)\right)$$
$$\Delta t(k) = \frac{\sqrt{\Delta x^2(k) + \Delta y^2(k)}}{V}$$
$$r(k) = \frac{d\psi}{dt}(k) \approx \frac{\psi(k+1) - \psi(k)}{\Delta t(k)}$$
$$\dot{r}(k) = \frac{dr}{dt}(k) \approx \frac{r(k+1) - r(k)}{\Delta t(k)}$$
$$u(k) = \frac{1}{K}\left(r(k) + T\dot{r}(k)\right). \qquad \text{(A.13)}$$

Fig. 37(b) and (c) illustrates lawnmower and box-spiral initial guesses, respectively, constructed using this clothoid method. Note that the inverse kinematic equations of (A.13) differentiate state trajectories using the forward Euler method, which requires small equally spaced time steps to ensure accuracy and feasibility of the derivatives. Small step size translates into a large number of nodes, which can drastically increase solver run time. The latter makes a compelling argument *against* supplying a deterministic search pattern for the initial guess.

ACKNOWLEDGMENT

The authors would like to thank the editor and two anonymous reviewers for their thoughtful comments and helpful suggestions.

REFERENCES

[1] S. Kragelund, C. Walton, and I. Kaminer, "Sensor-based motion planning for autonomous vehicle teams," in *Proc. MTS/IEEE OCEANS Conf.*, Monterey, CA, USA, 2016, pp. 1–8, doi: 10.1109/OCEANS.2016.7761183.

[2] A. Washburn and M. Kress, *Combat Modeling*, vol. 134. Berlin, Germany: Springer-Verlag, 2009.

[3] "Program Executive Office, Littoral and Mine Warfare, Expeditionary Warfare Directorate," *21st Century U.S. Navy Mine Warfare: Ensuring Global Access and Commerce*. Washington, DC, USA: Dept. Navy, Program Executive Off. Littoral Mine Warfare, 2009.

[4] D. Sternlicht, J. Fernandez, R. Holtzapple, D. Kucik, T. Montgomery, and C. Loeffler, "Advanced sonar technologies for autonomous mine countermeasures," in *Proc. MTS/IEEE OCEANS Conf.*, KONA, 2011, pp. 1–5, doi: 10.23919/OCEANS.2011.6107149.

[5] J. Keller, "Raytheon, applied physical sciences to develop Navy unmanned mine-hunting technology," Jun. 2, 2013. [Online]. Available: http://www.militaryaerospace.com/articles/2013/06/mine-hunting-USV.html. Accessed on: May 8, 2019.

[6] M. J. Bays, R. D. Tatum, L. Cofer, and J. R. Perkins, "Automated scheduling and mission visualization for mine countermeasure operations," in *Proc. MTS/IEEE OCEANS Conf.*, 2015, pp. 1–7, doi: 10.23919/OCEANS.2015.7401849.

[7] N. Abreu and A. Matos, "Minehunting mission planning for autonomous underwater systems using evolutionary algorithms," *Unmanned Syst.*, vol. 2, no. 4, pp. 323–349, Oct. 2014.

[8] B. Nguyen, D. Hopkin, and H. Yip, "Autonomous underwater vehicles: A transformation in mine counter-measure operations," *Defense Secur. Anal.*, vol. 24, no. 3, pp. 247–266, Sep. 2008.

[9] M. J. Bays, "Stochastic motion planning for applications in subsea survey and area protection," Ph.D. dissertation, Dept. Mech. Eng., Virginia Polytech. Inst. State Univ., Blacksburg, VA, USA, 2012.

[10] J. C. Hyland and C. M. Smith, "Automated area segmentation for ocean bottom surveys," in *Proc. SPIE 9454, Detection and Sensing of Mines, Explosive Objects, and Obscured Targets XX*, May 2015, Paper 94541N, doi: 10.1117/12.2179777.

[11] M. J. Bays, A. Shende, D. J. Stilwell, and S. A. Redfield, "Theory and experimental results for the multiple aspect coverage problem," *Ocean Eng.*, vol. 54, pp. 51–60, Nov. 2012.

[12] L. Paull, S. Saeedi, M. Seto, and H. Li, "Sensor-driven online coverage planning for autonomous underwater vehicles," *IEEE/ASME Trans. Mechatronics*, vol. 18, no. 6, pp. 1827–1838, Dec. 2013.

[13] B. Nguyen, M. J. Bays, A. Shende, and D. J. Stilwell, "An approach to subsea survey for safe naval transit," in *Proc. MTS/IEEE OCEANS Conf.*, KONA, 2011, pp. 1–6, doi: 10.23919/OCEANS.2011.6107225.

[14] C. Phelps, Q. Gong, J. O. Royset, C. Walton, and I. Kaminer, "Consistent approximation of a nonlinear optimal control problem with uncertain parameters," *Automatica*, vol. 50, no. 12, pp. 2987–2997, Dec. 2014.

[15] J. Foraker, J. O. Royset, and I. Kaminer, "Search-trajectory optimization: Part I, formulation and theory," *J. Optim. Theory Appl.*, vol. 169, no. 2, pp. 530–549, Jun. 2015.

[16] J. Foraker, J. O. Royset, and I. Kaminer, "Search-trajectory optimization: Part II, algorithms and computations," *J. Optim. Theory Appl.*, vol. 169, no. 2, pp. 550–567, Jun. 2015.

[17] C. Walton, C. Phelps, Q. Gong, and I. Kaminer, "A numerical algorithm for optimal control of systems with parameter uncertainty," in *Proc. 10th IFAC Symp. Nonlinear Control Syst.*, 2016, pp. 468–475.

[18] C. L. Walton, Q. Gong, I. Kaminer, and J. O. Royset, "Optimal motion planning for searching for uncertain targets," *IFAC Proc. Vol.*, vol. 47, no. 3, pp. 8977–8982, 2014.

[19] R. Stokey *et al.*, "Very shallow water mine countermeasures using the REMUS AUV: A practical approach yielding accurate results," in *Proc. MTS/IEEE OCEANS Conf.*, 2001, pp. 149–156.

[20] B. O. Koopman, "The theory of search—II. Target detection," *Oper. Res.*, vol. 4, no. 5, pp. 503–531, Oct. 1956.

[21] A. R. Washburn, *Search and Detection*, 4th ed., Linthicum, MD, USA: Inst. Oper. Res. Manage. Sci., 2002.

[22] D. H. Wagner, W. C. Mylander, and T. J. Sanders, Eds., *Naval Operations Analysis*, 3rd ed., Annapolis, MD, USA: Nav. Inst. Press, 1999.

[23] "REMUS 100 for defense applications," 2016. [Online]. Available: http://www.hydroid.com/remus-100-defense. Accessed on: Nov. 29, 2016.

[24] K. M. Kim, S. H. Lee, and J. N. Eagle, "Approximating the Poisson Scan and $(\lambda - \sigma)$ acoustic detection model with a random search formula," in *Proc. 40th Int. Conf. Comput. Ind. Eng.*, 2010, pp. 1–7, doi: 10.1109/ICCIE.2010.5668315.

[25] J. C. Foraker, "Optimal search for moving targets in continuous time and space using consistent approximations," Ph.D. dissertation, Dept. Oper. Res., Nav. Postgrad. School, Monterey, CA, USA, 2011.

[26] C. L. Walton, "The design and implementation of motion planning problems given parameter uncertainty," Ph.D. dissertation, Dept. Appl. Math. Statist., Univ. California, Santa Cruz, CA, USA, 2015.

[27] D. Sternlicht *et al.*, "Advanced sonar technologies for high clearance rate mine countermeasures," in *Proc. MTS/IEEE OCEANS Conf.*, Monterey, 2016, pp. 1–8, doi: 10.1109/OCEANS.2016.7761133.

[28] "Little USV, big applications," Apr. 2004. [Online]. Available: http://www.marinelink.com/news/applications-little-big323082. Accessed on: Oct. 23, 2016.

[29] D. Richman, "Seattle company builds boats with a mission: Navy and Coast Guard use remote-controlled Sea Fox," Seattle Post-Intelligencer, Seattle, WA, USA, Nov. 12, 2008. [Online]. Available: http://www.seattlepi.com/business/article/Seattle-company-builds-boats- with-a-mission-1291322.php. Accessed on: Dec. 3, 2013.

[30] A. Gadre, S. Kragelund, T. Masek, D. Stilwell, C. Woolsey, and D. Horner, "Subsurface and surface sensing for autonomous navigation in a riverine environment," in *Proc. Assoc. Unmanned Veh. Syst. Int.Unmanned Syst. North Amer. Conv.*, 2009, pp. 1192–1208.

[31] O. A. Yakimenko and S. P. Kragelund, "Real-time optimal guidance and obstacle avoidance for UMVs," in *Autonomous Underwater Vehicles*, N. A. Cruz, Ed. Rijeka, Croatia: InTech, 2011. [Online]. Available: http://www.intechopen.com/books/autonomous-underwater-vehicles/real-tim e-optimal-guidance-and-obstacle-avoidance-for-umvs

[32] S. Kragelund, V. Dobrokhodov, A. Monarrez, M. Hurban, and C. Khol, "Adaptive speed control for autonomous surface vessels," in *Proc. MTS/IEEE OCEANS Conf.*, 2013, pp. 1–10, doi: 10.23919/OCEANS.2013.6741115.

[33] S. Terjesen, "Navigation system design and state estimation for a small rigid hull inflatable boat (RHIB)," Master's thesis, Dept. Mech. Aerosp. Eng., Nav. Postgrad. School, Monterey, CA, USA, 2014.

[34] T. I. Fossen, *Marine Control Systems Guidance, Navigation, and Control of Ships, Rigs and Underwater Vehicles*. Trondheim, Norway: Marine Cybernetics, 2002.

[35] L. Moreira, T. I. Fossen, and C. G. Soares, "Modeling, Guidance and Control of 'Esso Osaka' Model," *IFAC Proc. Vol.*, vol. 38, no. 1, pp. 85–90, 2005.

[36] J. Journee, "A simple method for determining the manoeuvring indices K and T from zigzag trial data," Delft Univ. Technol., Ship Hydromech. Lab., Delft, Tech. Rep. 267, Jun. 1970. [Online]. Available: http://shipmotions.nl/DUT/PapersReports/. Accessed on: Oct. 24, 2016.

[37] D. Clarke, "The foundations of steering and maneuvering," in *Proc. 6th Conf. Maneuvering Control Mar. Crafts*, 2003, pp. 2–16.

[38] C. Sonnenburg *et al.*, "Control-oriented planar motion modeling of unmanned surface vehicles," Virginia Center Auton. Syst, Virginia Tech, Blacksburg, VA, USA, Tech. Rep. VACAS-2010-01, 2010. [Online]. Available: http://www.unmanned.vt.edu/discovery/reports/VaCAS_2010_01.pdf. Accessed on: July 17, 2016.

[39] C. von Alt, B. Allen, T. Austin, and R. Stokey, "Remote environmental measuring units," in *Proc. Symp. Auton. Underwater Veh. Technol.*, 1994, pp. 13–19.

[40] C. von Alt *et al.*, "Hunting for mines with REMUS: A high performance, affordable, free swimming underwater robot," in *Proc. MTS/IEEE OCEANS Conf.*, 2001, pp. 117–122.

[41] "REMUS," Oceanogr. Syst. Lab, Woods Hole Oceanogr. Inst., Woods Hole, MA, USA. 2016. [Online]. Available: http://www.whoi.edu/main/remus. Accessed on: Nov. 29, 2016.

[42] "Mine countermeasure applications," 2015. [Online]. Available: http://www.hydroid.com/product-applications/12/mine-countermeasures. Accessed on: Nov. 29, 2016.

[43] D. Horner, A. Healey, and S. Kragelund, "AUV experiments in obstacle avoidance," in *Proc. MTS/IEEE OCEANS Conf.*, 2005, pp. 1464–1470.

[44] D. Horner and O. Yakimenko, "Recent developments for an obstacle avoidance system for a small AUV," *IFAC Proc. Vol.*, vol. 40, no. 17, pp. 19–25, 2007.

[45] D. Horner, N. McChesney, T. Masek, and S. Kragelund, "3D reconstruction with an AUV mounted forward-looking sonar," in *Proc. Int. Symp. Unmanned Untethered Submersible Technol.*, 2009, pp. 393–401.

[46] D. Sgarioto, "Control system design and development for the REMUS autonomous underwater vehicle," Def. Technol. Agency, Auckland, New Zealand, Tech. Rep. DTA Report 240, May 2007.

[47] "Beta distribution," MathWorks. 2016. [Online]. Available: https://www.mathworks.com/help/stats/beta-distribution.html. Accessed on: Nov. 29, 2016.

[48] A. Washburn, "Katz distributions and minefield clearance," *Mil. Oper. Res. J.*, vol. 11, no. 3, pp. 63–74, Jan. 2006. [Online]. Available: https://www.mors.org/Publications/MOR-Journal/Online-Issues

[49] W. R. Monach and J. E. Baker, "Estimating risk to transiting ships due to multiple threat mine types," *Mil. Oper. Res. J.*, vol. 11, no. 3, pp. 35–47, Jun. 2006. [Online]. Available: https://www.mors.org/Publications/MOR-Journal/Online-Issues

[50] M. J. Bays, A. Shende, and D. J. Stilwell, "Multi-agent motion planning using Bayes risk," *Robot. Auton. Syst.*, vol. 86, pp. 1–12, Dec. 2016. [Online]. Available: https://linkinghub.elsevier.com/retrieve/pii/S0921889016304869

[51] B. O. Koopman, *Search and Screening*. Washington, DC, USA: Oper. Eval. Group, Off. Chief N. Oper., Navy Dept., 1946.

[52] B. O. Koopman, *Search and Screening : General Principles With Historical Applications*. New York, NY, USA: Pergamon, 1980.

[53] L. D. Stone, J. O. Royset, and A. R. Washburn, *Optimal Search for Moving Targets*, vol. 237. Berlin, Germany: Springer-Verlag, 2016.

[54] P. E. Gill, W. Murray, and M. A. Saunders, *Users Guide for SNOPT Version 6: A Fortran Package for Large-Scale Nonlinear Programming*, 2002. [Online]. Available: http://www.cam.ucsd.edu/peg/papers/sndoc6.pdf. Accessed on: Sep. 30, 2018.

[55] S. P. Kragelund, "Optimal sensor-based motion planning for autonomous vehicle teams," Ph.D. dissertation, Nav. Postgrad. School, Monterey, CA, USA, Mar. 2017. [Online]. Available: https://calhoun.nps.edu/handle/10945/53003

[56] C. Phelps, Q. Gong, J. Royset, and I. Kaminer, "Consistent approximation of an optimal search problem," in *Proc. IEEE Conf. Decis. Control*, 2012, pp. 630–637.

[57] I. M. Ross, "Astrodynamic Optimization," Dept. Mech. Aerosp. Eng., Nav. Postgrad. School, Monterey, CA, USA, 2010 (class notes for AE4850).

[58] M. A. Hurni, "An information-centric approach to autonomous trajectory planning utilizing optimal control techniques," Ph.D. dissertation, Dept. Mech. Aerosp. Eng., Nav. Postgrad. School, Monterey, CA, USA, 2009.

[59] A. E. Bryson, *Applied Optimal Control: Optimization, Estimation and Control*. Washington, DC, USA: Hemisphere Pub. Corp., 1975.

[60] T. L. Vincent and W. J. Grantham, *Nonlinear and Optimal Control Systems*, 1st ed., Hoboken, NJ, USA: Wiley, 1999.

[61] A. L. Peressini, F. E. Sullivan, and J. J. J. Uhl, *The Mathematics of Nonlinear Programming*. Berlin, Germany: Springer-Verlag, Jun. 1993.

[62] T. Eiter and H. Mannila, "Computing discrete Fréchet distance," Auckland, New Zealand Technische Universität Wien, Vienna, Austria, Tech. Rep. CD-TR 94/64, 1994. [Online]. Available: http://www.kr.tuwien.ac.at/staff/eiter/et-archive/cdtr9464.pdf. Accessed on: Oct. 28, 2016.

[63] H. Alt and L. Scharf, "Computing the Hausdorff distance between curved objects," *Int. J. Comput. Geom. Appl.*, vol. 18, no. 4, pp. 307–320, 2008.

[64] R. E. Keenan, "An introduction to GRAB eigenrays and CASS reverberation and signal excess," in *Proc. MTS/IEEE OCEANS Conf.*, 2000, pp. 1065–1070.

[65] H. Weinberg, R. Deavenport, E. McCarthy, and C. Anderson, "Comprehensive Acoustic System Simulation (CASS) Reference Guide," Nav. Undersea Warfare Center Division, Newport, RI, USA, Tech. Rep. NUWC-NPT TM 01-016, Mar. 2001.

[66] P. Etter, *Underwater Acoustic Modeling and Simulation*, 4th ed., New York, NY, USA: Taylor Francis, 2013.

[67] S. B. Dasinger, B. I. Incze, and T. A. Holz, "A concept for efficient signal excess calculation for multistatic operations analysis," in *Proc. OCEANS—Asia Pac.*, 2006, pp. 1–6, doi: 10.1109/OCEANSAP.2006.4393977.

[68] A. D. Waite, *Sonar for Practising Engineers*, 3rd ed., Hoboken, NJ, USA: Wiley, 2002.

[69] T. BlueView, "P450 Series 2D Imaging Sonar," 2015. [Online]. Available: http://www.teledynemarine.com/Lists/Downloads/p450-datasheet-hr.pdf. Accessed on: Sep. 26, 2019.

[70] T. BlueView, "P900 Series 2D Imaging Sonar," 2015. [Online]. Available: http://www.teledynemarine.com/Lists/Downloads/p900-datasheet-hr.pdf. Accessed on: Sep. 26, 2019.

[71] "Sea Scan SSPC AUV system." 2013. [Online]. Available: http://www.marinesonic.com/products/seascanSSPCAUV.html. Accessed on: Nov. 29, 2016.

[72] R. J. Urick, *Principles of Underwater Sound*, 3rd ed., Los Altos, CA, USA: Peninsula, 1996.

[73] "SCOUT MKII AUV—Marine Sonic Technology," 2018. [Online]. Available: https://www.marinesonic.com/arc-scout-mkii

[74] EdgeTech Resource Center, 2016. [Online]. Available: https://www.edgetech.com/resource-center/

[75] M. Ainslie, *Principles of Sonar Performance Modelling*. Berlin, Germany: Springer-Verlag, 2010.

[76] P. C. Chu, C. Cintron, S. D. Haeger, and R. E. Keenan, "Acoustic mine detection using the Navy's CASS/GRAB model," in *Proc. J. Counter-Ordnance Technol. (5th Int. Symp. Technol. Mine Problem)*, 2002. [Online]. Available: http://www.dtic.mil/cgi-bin/GetTRDoc?Location=U2&doc=GetTRDoc.pdf&AD=ADA478751

[77] P. C. Chu, N. A. Vares, and R. E. Keenan, "Uncertainty in acoustic mine detection due to environmental variability," in *Proc. J. Counter-Ordnance Technol. (6th Int. Symp. Technol. Mine Problem)*, 2004. [Online]. Available: http://www.dtic.mil/cgi-bin/GetTRDoc?Location=U2&doc=GetTRDoc.pdf&AD=ADA482282. Accessed on: Apr. 21, 2016.

[78] R. E. Hansen, "Introduction to synthetic aperture sonar," in *Sonar Systems*, N. Kolev, Ed. Rijeka, Croatia: InTech, 2011. [Online]. Available: http://www.intechopen.com/books/sonar-systems/introduction-to-synthetic-aperture-sonar. Accessed on: Oct. 17, 2016.

[79] G. W. Pollitt, "Mine countermeasures (MCM) tactical decision aids (TDAs): A historical review," *Mil. Oper. Res. J.*, vol. 11, no. 3, pp. 7–17, Jun. 2006. [Online]. Available: https://www.mors.org/Publications/MOR-Journal/Online-Issues

[80] "Mine Warfare," Off. Chief Nav. Oper., Dept. Navy, Norfolk, VA, USA: Naval Warfare Publication NWP 3-15, Aug. 1996.

[81] A. Ivanov, "Fractional activation functions in feedforward artificial neural networks," in *Proc. 20th Int. Symp. Elect. App. Technol.*, 2018, pp. 1–4, doi: 10.1109/SIELA.2018.8447139.

[82] E. W. Weisstein, "Sigmoid function," 2016. [Online]. Available: http://mathworld.wolfram.com/SigmoidFunction.html. Accessed on: Nov. 29, 2016.

[83] P. Blondel, *The Handbook of Sidescan Sonar*. Berlin, Germany: Springer-Verlag, 2009.

[84] S. D. Anstee, "The effects of towfish motion on sidescan sonar images," DSTO Mater. Res. Lab., Melbourne, VIC, Australia, Tech. Rep. MRL-RR-1-94, 1994. [Online]. Available: http://digext6.defence.gov.au/dspace/handle/1947/9915. Accessed on: Jun. 3, 2016.

[85] C. Loeffler, "Sonar and AUV technology," Off. Ocean Exploration Res., Nat. Ocean. Atmos. AdminSilver Spring, MD, USA. 2010. [Online]. Available: http://oceanexplorer.noaa.gov/explorations/10thunderbay/background/sonar/sonar.html. Accessed on: Nov. 29, 2016.

[86] L. Moreavek and T. Brudner, "USS Asheville leads the way in high frequency sonar," *Undersea Warfare*, vol. 1, no. 3, pp. 22–24, 1999. [Online]. Available: http://www.public.navy.mil/subfor/underseawarfaremagazine/Issues/Archives/issue_03/uss_asheville.htm

[87] R. L. Thompson, J. Seawall, and T. Josserand, "Two dimensional and three dimensional imaging results using blazed arrays," in *Proc. MTS/IEEE OCEANS Conf.*, 2001, pp. 985–988.

[88] N. A. McChesney, "Three-dimensional feature reconstruction with dual forward looking sonars for unmanned underwater vehicle navigation," Master's thesis, Dept. Elect. Eng., Nav. Postgrad. School, Monterey, CA, USA, 2009.

[89] "Multibeam sonar theory of operation," L3 Commun. SeaBeam Instrum., East Walpole, MA, USA, 2000. [Online]. Available: https://www.ldeo.columbia.edu/res/pi/MB-System/sonarfunction/SeaBeamMultibeamTheoryOperation.pdf. Accessed on: Oct. 20, 2016.

[90] S. T. Bachelor, R. L. Thompson, and J. Seawall, "Systems and methods implementing frequency-steered acoustic arrays for 2D and 3D imaging," U.S. Patent 7606114, Oct. 20, 2009. [Online]. Available: http://patft.uspto.gov/netacgi/nph-Parser?Sect1=PTO2&Sect2=HITOFF&p=1&u=%2Fnetahtml%2FPTO%2Fsearch-bool.html&r=5&f=G&l=50&co1=AND&d=PTXT&s1=7606114&OS=7606114&RS=7606114

[91] C. Jones, "Teledyne Blueview P-Series Sonar Maximum Source Level Analysis," Teledyne BlueView, Seattle, WA, USA, Nov. 2012, White Paper. [Online]. Available: http://www.teledynemarine.com/Lists/Downloads/P-Series-Max-Source-Level-Analysis-White-Paper-Teledyne-BlueView.pdf. Accessed on: Jun. 17, 2020.

[92] T. E. Wilcox and B. Fletcher, "High frequency side scan sonar for target reacquisition and identification," in *Proc. MTS/IEEE OCEANS Conf.*, 2003, pp. 1882–1887.

[93] H. Choset, "Coverage for robotics—A survey of recent results," *Ann. Math. Artif. Intell.*, vol. 31, no. 1, pp. 113–126, Oct. 2001.

[94] E. Galceran and M. Carreras, "A survey on coverage path planning for robotics," *Robot. Auton. Syst.*, vol. 61, no. 12, pp. 1258–1276, 2013.

[95] P. Cheng, J. Keller, and V. Kumar, "Time-optimal UAV trajectory planning for 3D urban structure coverage," in *Proc. IEEE/RSJ Int. Conf. Intell. Robots Syst.*, 2008, pp. 2750–2757.

[96] J. R. Stack and C. M. Smith, "Combining random and data-driven coverage planning for underwater mine detection," in *Proc. MTS/IEEE OCEANS Conf.*, 2003, pp. 2463–2468.

[97] A. Percival and M. Stoddard, "PATHA: A planning aid for tasking heterogeneous assets for route survey or mine countermeasures operations," in *Proc. MTS/IEEE OCEANS Conf.*, Seattle, WA, USA, 2010, pp. 1–8, doi: 10.1109/OCEANS.2010.5664551.

[98] I. M. Ross, "A beginner's guide to DIDO: A MATLAB application package for solving optimal control problems," Elissar, Carmel, CA, USA, Tech. Rep. TR-711, 2007. [Online]. Available: www.elissarglobal.com

[99] E. M. Arkin, S. P. Fekete, and J. S. B. Mitchell, "Approximation algorithms for lawn mowing and milling," *Comput. Geom.*, vol. 17, no. 1, pp. 25–50, Oct. 2000.

[100] W. H. Huang, "Optimal line-sweep-based decompositions for coverage algorithms," in *Proc. IEEE Int. Conf. Robot. Autom.*, 2001, pp. 27–32.

[101] P.-M. Hsu and C.-L. Lin, "Optimal planner for lawn mowers," in *Proc. IEEE 9th Int. Conf. Cybern. Intell. Syst.*, 2010, pp. 1–7, doi: 10.1109/UKRICIS.2010.5898126.

[102] G. T. Huntington *et al.*, "A comparison of accuracy and computational efficiency of three pseudospectral methods," in *Proc. AIAA Guid., Navig., Control Conf.*, 2007, pp. 1–25, doi: 10.2514/6.2007-6405.

[103] L. Trefethen, *Spectral Methods in MATLAB* (Software, Environments and Tools). Philadelphia, PA, USA: SIAM, 2000.

[104] I. M. Ross and M. Karpenko, "A review of pseudospectral optimal control: From theory to flight," *Annu. Rev. Control*, vol. 36, no. 2, pp. 182–197, Dec. 2012.

[105] Q. Gong, I. M. Ross, W. Kang, and F. Fahroo, "Connections between the covector mapping theorem and convergence of pseudospectral methods for optimal control," *Comput. Optim. Appl.*, vol. 41, no. 3, pp. 307–335, Dec. 2008.

[106] "Intel Xeon processor specifications," Intel, Santa Clara, CA, USA. 2013. [Online]. Available: http://ark.intel.com/products/81060/Intel-Xeon-Processor-E5-2698-v3-40M -Cache-2_30-GHz. Accessed on: Nov. 14, 2016.

[107] A. J. Healey and J. Kim, "Bugs: Robot control, UXO and minefield clearance," Mech. Eng. Dept., Nav. Postgrad. School, Monterey, CA, USA, Tech. Rep. NPS-ME-96-005, Dec. 1996. [Online]. Available: http://calhoun.nps.edu/bitstream/handle/10945/24446/NPS-ME-96-005.pdf?sequence=1&isAllowed=y

[108] V. Ablavsky and M. Snorrason, "Optimal search for a moving target—A geometric approach," in *Proc. AIAA Guid., Navig., Control Conf.*, 2000, pp. 1–9, doi: 10.2514/6.2000-4060.

[109] M. Dille and S. Singh, "Efficient aerial coverage search in road networks," in *Proc. AIAA Guid., Navig., Control Conf.*, 2013, Paper AIAA 2013-5094, pp. 1–20, doi: 10.2514/6.2013-5094.

[110] A. Sriraman and M. Bays, "Efficient reacquire and identify path planning over large areas," in *Proc. OCEANS Conf.*, St. John's, NL, Canada, 2014, pp. 1–7, doi: 10.1109/OCEANS.2014.7003087.

[111] J. Haugen, "Guidance algorithms for planar path-based motion control scenarios," Master's thesis, Dept. Eng. Cybern., Norwegian Univ. Sci. Technol., Trondheim, Norway, 2010.

Sean Kragelund received the B.S. degree in mechanical engineering from Santa Clara University, Santa Clara, CA, USA, in 1995, the M.S. degree in electrical engineering from the University of Washington, Seattle, WA, USA, in 2002, and the Ph.D. degree in mechanical engineering from the Naval Postgraduate School, Monterey, CA, USA, in 2016.

From 1996 to 2000, he was with Boeing Commercial Airplanes. From 2001 to 2002, he was was with the Autonomous Flight Systems Laboratory, University of Washington, Seattle, WA, USA. He began working for the U.S. Navy in 2002, first with the Naval Undersea Warfare Center, Keyport, WA, USA and then he has been with the Naval Postgraduate School's Center for Autonomous Vehicle Research since 2005. He is currently a Research Assistant Professor with the Department of Mechanical and Aerospace Engineering, Naval Postgraduate School, Monterey. His research interests include guidance, navigation, and control for teams of unmanned aerial, surface, and underwater vehicles.

Claire Walton received the B.S. degree in mathematics from the California Institute of Technology, Pasadena, CA, USA, in 2005 and the Ph.D. degree in applied mathematics and statistics from the University of California, Santa Cruz, CA, USA, in 2015.

She received a National Research Council Fellowship for postdoctoral studies from 2015 to 2018 and is currently a Research Assistant Professor with the Department of Mechanical and Aerospace Engineering, Naval Postgraduate School, Monterey, CA, USA. Her research interests include computational optimal control, pseudospectral methods, uncertainty quantification, and autonomous vehicle guidance.

Isaac Kaminer received the B.S. degree in electrical engineering in 1983 and the M.S. degree in electrical engineering in 1985, both from the University of Minnesota, Minneapolis, MN, USA, and the Ph.D. degree in electrical engineering from the University of Michigan, Ann Arbor, MI, USA in 1992.

Prior to it he spent four years working at Boeing Commercial Airplanes, first as a Control Engineer in the 757/767/747-400 Flight Management Computer Group and then as an Engineer in the Flight Control Research Group. Since 1992, he has been with the Naval Postgraduate School, Monterey, CA, USA, first at the Aeronautics and Astronautics Department and currently with the Department of Mechanical and Aerospace Engineering, where he is a Professor. He has more than 20 years of experience developing and flight testing new guidance, navigation, and control algorithms for both manned and unmanned aircraft. His more recent efforts have focused on the development of coordinated control strategies for multiple UAVs and adversarial swarming. He has coauthored more than 150 refereed publications. His research has been supported by ONR, NASA, USAF, U.S. Army, NAVAIR, and USSOCOM.

Vladimir Dobrokhodov received the M.S. degree in aerospace engineering from the Moscow Aviation Institute, Russia, in 1991, the M.S. degree in operations research in 1993 and the Ph.D. degree in aerospace engineering in 1999, both from the Zhukovsky Air Force Engineering Academy, Moscow, Russia.

Since 2001, he has been with the Naval Postgraduate School, Monterey, CA, USA, first as a National Research Council Postdoctoral Awardee and then, since 2004, as a Faculty Member. He is currently an Associate Professor with the Department of Mechanical and Aerospace Engineering. He has more than 20 years of experience in the development and flight validation of novel guidance, navigation, and control algorithms focused on advancing the onboard intelligence of unmanned systems. He has authored or coauthored more than 100 refereed publications on research projects sponsored by ONR, NASA, USAF, OSD, DHS, NAVAIR, and USSOCOM.